nature communications

Article

https://doi.org/10.1038/s41467-024-55554-7

Enhanced motivated behavior mediated by pharmacological targeting of the FGF14/$Na_v1.6$ complex in nucleus accumbens neurons

Received: 30 March 2024

Accepted: 17 December 2024

Published online: 02 January 2025

Check for updates

A list of authors and their affiliations appears at the end of the paper

Protein/protein interactions (PPI) play crucial roles in neuronal functions. Yet, their potential as drug targets for brain disorders remains underexplored. The fibroblast growth factor 14 (FGF14)/voltage-gated Na^+ channel 1.6 ($Na_v1.6$) complex regulates excitability of medium spiny neurons (MSN) of the nucleus accumbens (NAc), a central hub of reward circuitry that controls motivated behaviors. Here, we identified compound 1028 (IUPAC: ethyl 3-(2-(3-(hydroxymethyl)-1*H*-indol-1-yl)acetamido)benzoate), a brain-permeable small molecule that targets $FGF14^{R117}$, a critical residue located within a druggable pocket at the FGF14/$Na_v1.6$ PPI interface. We found that 1028 modulates FGF14/$Na_v1.6$ complex assembly and depolarizes the voltage-dependence of $Na_v1.6$ channel inactivation with nanomolar potency by modulating the intramolecular interaction between the III-IV linker and C-terminal domain of the $Na_v1.6$ channel. Consistent with the compound's effects on $Na_v1.6$ channel inactivation, 1028 enhances MSN excitability ex vivo and accumbal neuron firing rate in vivo in murine models. Systemic administration of 1028 maintains behavioral motivation preferentially during motivationally deficient conditions in murine models. These behavioral effects were abrogated by in vivo gene silencing of *Fgf14* in the NAc and were accompanied by a selective reduction in accumbal dopamine levels during reward consumption in murine models. These findings underscore the potential to selectively regulate complex behaviors associated with neuropsychiatric disorders through targeting of PPIs in neurons.

Protein/protein interactions (PPI) are involved in cellular functions ranging from intracellular signaling to apoptosis, making them crucial targets for therapeutic development[1]. Unlike receptors and enzymes with well-defined binding pockets[2], PPIs typically lack deep cavities, posing challenges for small molecule modulation. Despite this difficulty[2], their orthogonality to conventional drug targets has motivated PPI drug discovery campaigns to meet the need for the development of medications with diminished side effects[3]. However, while PPI targeting drugs have gained FDA approval for HIV[4] and cardiovascular disease[5], and are being investigated as anti-neoplastic agents in clinical trials[6], their exploration in central nervous system (CNS) drug discovery remains limited.

In neurons, PPIs regulate functions including neurotransmission, neurogenesis, synaptogenesis, synaptic plasticity, and intrinsic excitability[7]. Pertinent to intrinsic excitability, the PPI between the voltage-gated Na^+ (Na_v) channel isoform 1.6 and its auxiliary protein

e-mail: felaezza@utmb.edu

fibroblast growth factor 14 (FGF14) plays critical roles in controlling the Na^+ current and output of neurons[8,9]. In the nucleus accumbens (NAc), which is a central hub of the mesolimbic reward circuit[10], this PPI is especially crucial, as both proteins are abundantly expressed[11,12] and FGF14/Na_v1.6 complex assembly controls the action potential firing of medium spiny neurons (MSN)[11]. MSNs are GABAergic and the principal cells of the NAc, comprising ~95% of the total cell volume and providing the sole output of the brain region[13]. MSNs confer regulation of dopamine (DA) signaling in the NAc through direct and indirect connections with interneurons and dopaminergic cells in the ventral tegmental area (VTA)[14], and by modulating local circuit components within the NAc, such as those involving cholinergic interneuron (CIN) regulation of local DA release[15–17]. This regulation of DA signaling in the NAc by MSNs exerts a profound influence on reward circuitry and motivated behaviors[18,19]. Given this salient function of MSN activity in regulating motivated behaviors, coupled with perturbations of NAc activity being implicated in the pathophysiology of major depression[20–22], pharmacological targeting of accumbal MSNs represents a promising therapeutic approach for neuropsychiatric disorders.

Based upon this premise, we sought to develop small molecule modulators of FGF14/Na_v1.6 complex assembly as a strategy to control accumbal MSN activity and regulate motivated behaviors. To that end, we employed a multi-tiered screening platform including primary, secondary, orthogonal, and functional assays complemented by a lead optimization campaign, as well as in vivo gene silencing for target validation and fiber photometry measurement of NAc dopamine release in rodent models of reward-seeking behavior.

Results

High-throughput screening of small molecule modulators of the FGF14/Na_v1.6 complex

To identify small molecules able to specifically modulate FGF14/Na_v1.6 complex formation, we screened ~45,000 commercially available small molecules from the Maybridge and Chembridge libraries against the complex by using a previously validated split-luciferase complementation assay (LCA) that allows reconstitution of the FGF14/Na_v1.6 C-terminal domain (CTD) complex in living cells[23]. The small molecules screened and otherwise employed in this study comply with previously described criteria of chemical probes[24]. A diagrammatic representation of the screening funnel is shown in Fig. 1a. The initial screening was performed in singlicate, and two unbiased methods were used to select hits. The first method used Z-scores (Cut-offs: $Z \geq 4$ or $Z \leq -5$), which were calculated using on-plate controls (0.3% DMSO, $n = 16$ per plate). This method identified 1185 hits that were nontoxic (Fig. 1b, d). Of the 1185 compounds that were nontoxic and met the Z-score cut-off, we eliminated the 225 lowest-ranking compounds (i.e., those with the lowest Z-score above the cut-off) and proceeded with re-screening the 960 compounds with the highest Z-score above the cut-off in triplicate. After re-screening the 960 highest ranking compounds based upon Z-score in triplicate, we did a second analysis of the initial screening of 44,480 compounds in singlicate using a B-score method (Cut-offs: $B \geq 12$ or $B \leq -14$), which were calculated using an algorithm that accounted for plate and batch effects irrespective of per plate controls[25]. The method identified an additional 224 hits that were nontoxic (Fig. 1c, d). These 224 additional hits identified via the B-score method were then screened in triplicate. Thus, combining the 960 highest-ranked compounds based on the Z-score and the 224 hits that met the B-score cutoff, 1184 compounds were screened in triplicate. Of these 1184 compounds that were re-screened in triplicate, the modulatory effects of 544 compounds on FGF14/Na_v1.6 complex assembly were confirmed (Fig. 1e). The remaining 544 compounds were then counter-screened against the full-length *P. pyralis* luciferase enzyme in transiently transfected HEK293 cells to identify potential false positives interfering with the luciferase reporter system. Using cut-offs of $Z \geq -3$, this assay identified 152 false positives (148 from Z-score set, 4 from B-score set) that were excluded from further studies (Fig. 1f). The remaining 392 compounds were then stratified by structural and chemical properties, and those compounds exhibiting undesirable moieties (i.e., Pan-Assay Interference Compounds (PAINS)[26], violation of Lipinski's Rule of 5[27]) were excluded, leaving a remaining candidate pool of 70 compounds (40 from the Z-score set, 30 from the B-score set). While both inhibitors and enhancers were identified as leads in the primary assay, enhancers that had been identified and remained at this juncture in the screening funnel displayed undesirable structural and chemical properties for CNS drug discovery, leaving the remaining pool of candidate compounds featuring only inhibitors. The dose dependency of the effects of these 70 compounds on the FGF14/Na_v1.6 complex was then assessed. Analysis of the dose-response functions of the 70 remaining compounds identified 16 compounds with low micromolar potency (Fig. 1g).

The 16 remaining hits, the chemical structures of which are shown in Supplementary Fig. S1, were next repurchased. We first re-screened the 16 repurchased hits to validate their observed biological activity. Notably, consistent with their effects observed in the initial HTS described above, all 16 hits displayed dose-dependent effects on FGF14/Na_v1.6 complex assembly (Supplementary Fig. S2) with potencies ranging from 0.97 μM – 21.78 μM (Supplementary Table S1). We next assessed the selectivity of compounds for the FGF14/Na_v1.6 complex. To do so, we counter-screened the top 16 hits at 50 μM against other previously demonstrated Na_v channel/iFGF pairs, including FGF13/Na_v1.6[28], FGF14/Na_v1.2[29], and the FGF14/FGF14 homodimer[30]. This screening identified 7 hits with selective effects on FGF14/Na_v1.6 complex assembly (Fig. 2a), which were subsequently evaluated for binding toward FGF14 and the Na_v1.6 CTD using two methods. The first method was a protein thermal shift (PTS) assay, which uses changes in melting temperature (ΔT_m) as a readout of protein/ligand binding. This method identified two compounds that failed to meet the ΔT_m cutoff of ± 2 °C (Fig. 2b), thereby narrowing the candidate pool down to 5 compounds. The protein/ligand binding relationships of these 5 compounds with FGF14 and the Na_v1.6 CTD were then quantitatively assessed using surface plasmon resonance (SPR). These SPR studies revealed that all 5 compounds bound FGF14, Na_v1.6 CTD, or both (Fig. 2c), and the protein/ligand binding data of the 7 compounds in the two assays is summarized in Supplementary Tables 2 and 3. While it is potentially somewhat surprising that 3 of the 5 compounds (i.e., 5674, 7605, and 7647) bind to both FGF14 and the Na_v1.6 CTD, this is consistent with what we have previously reported for peptidomimetics targeting the FGF14/Na_v1.6 complex[31,32] and with the characteristics of PPI modulators, which often bind at the PPI interface with multiple contact points, bridging both proteins to either stabilize or disrupt the interaction[33].

Lead optimization and identification of 1028, a modulator of the FGF14/Na_v1.6 complex with high nanomolar potency

Previous reports have indicated that ideal leads for central nervous system drug discovery have a total polar surface area of less than 75 $Å^2$ and a molecular weight of less than 400 g/mol[34]. Of the remaining compounds, only 7605 (Fig. 3a) met these criteria. In line with 7605 meeting these aforementioned criteria for ideal leads for CNS drug discovery[34], an in silico blood-brain barrier (BBB) permeability screening predicted that the compound was BBB penetrant (Supplementary Fig. S3). However, 7605 displayed poor aqueous solubility, which would limit concentrations that could be administered in vivo. To remedy this shortcoming of 7605, the 3-methyl group on the phenyl ring of 7605 was modified as a 3-carboxylic acid ethyl ester moiety, which produced the analog called 1028 (AKA PW1028; IUPAC: ethyl 3-(2-(3-(hydroxymethyl)-1*H*-indol-1-yl)acetamido)benzoate; Fig. 3b). Compound 1028 was evaluated using the LCA, which revealed that the 7605 analog displayed a potency of 240 ± 31 nM (Fig. 3c), roughly 4–5 times more

https://doi.org/10.1038/s41467-024-55554-7

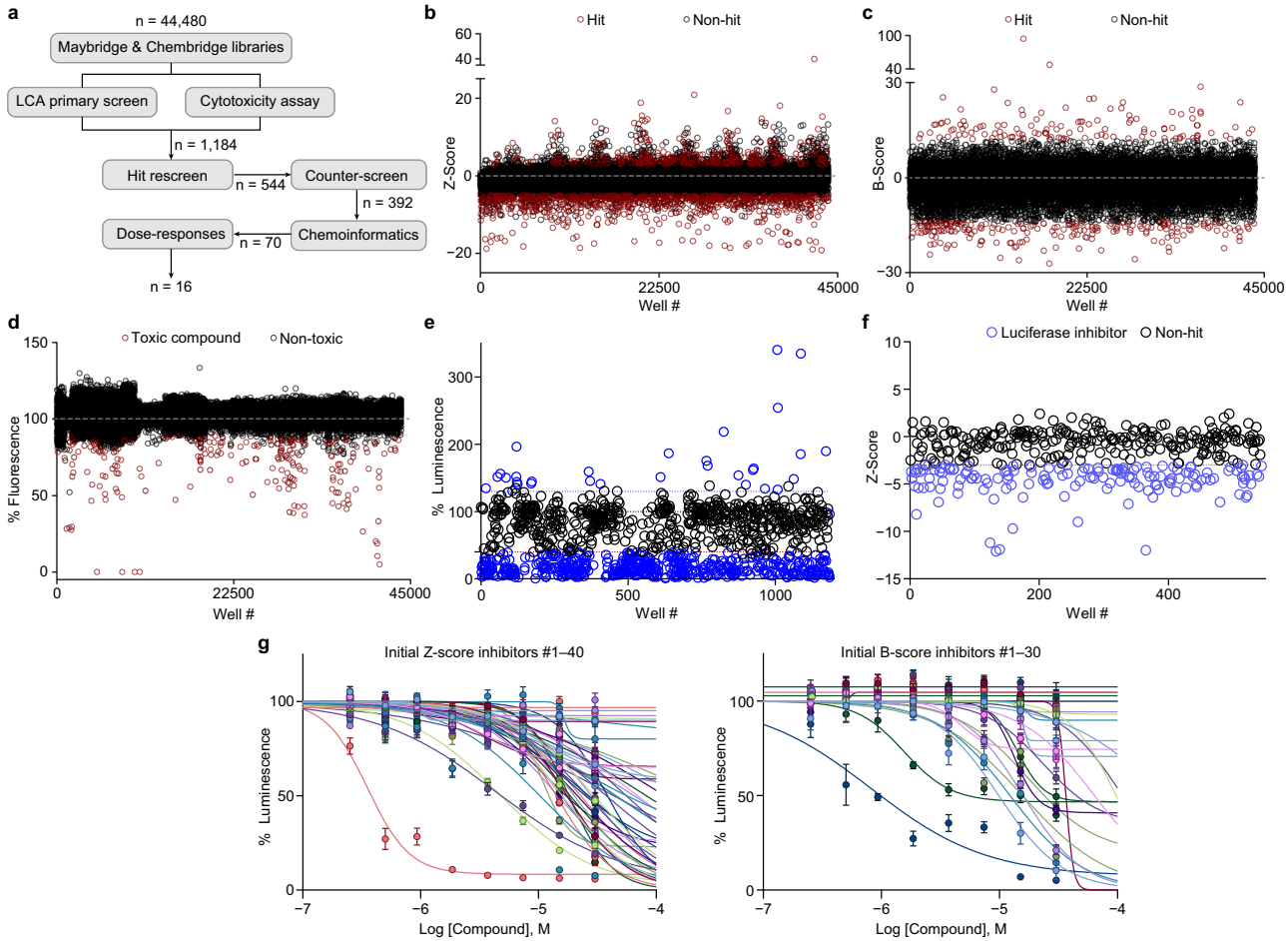

Fig. 1 | High throughput screening of small molecules against the FGF14/Na$_v$1.6 complex assembly. a Pipeline summarizing the initial HTS. **b**, **c** Z-scores (**b**) and B-scores (**c**) for all compounds screened using the LCA. **d** All compounds were evaluated for cellular toxicity using the fluorescence-based CTB assay immediately following LCA screening. **e** 1184 preliminary hits based on both B-scores and Z-scores were re-screened in triplicate using the LCA, and mean % maximal luminescence is shown. Hits taken to the next stage were determined by a combination of Z-score (cut off: $Z \geq 3$ or $Z \leq -4$) and relative luminescence (cut off: % lum ≥ 130% or % lum ≤ 40% for). **f** 544 hits remaining after triplicate rescreen were validated by full-length luciferase assay to identify false positives (i.e., affect luminescence in the LCA via modulation of the luciferase enzyme rather than FGF14 or Na$_v$1.6). 152 compounds significantly inhibited luminescence ($Z \leq -3$; shown as purple) and were eliminated at this stage. **g** Following manual inspection of hit chemical structures, dose responses using the LCA were performed for the remaining 70 compounds (40 and 30 hits each from the Z-score and B-score hit set, respectively) with the greatest potential for blood-brain barrier permeability. In (**g**), error bars represent SD. Source data are provided as a Source Data file.

potent than the parental compound. Consistent with the compound's in-cell potency, compound 1028 displayed a K_D toward FGF14 of 293 ± 81 nM (Fig. 3d), but no detectable binding to the Na$_v$1.6 CTD (Fig. 3e), as assessed by SPR. 1028's lack of binding to the Na$_v$1.6 CTD is dissimilar to the parental 7605, which binds to both FGF14 and the Na$_v$1.6 CTD. In our previous works using peptidomimetics targeting the FGF14/Na$_v$1.6 complex, we have similarly observed that analogs derived from the same parental structure display binding to either FGF14 alone or binding to both FGF14 and the Na$_v$1.6 CTD[31,32]. In Wang et al.[31], we showed that while the addition of an N-terminal 1-adamatanecarbonyl pharmacophore to the PLEV tetrapeptide produced analogs with high affinity binding to FGF14, modification of the moieties at the C-terminal end of the tetrapeptide dictated binding to the Na$_v$1.6 CTD. In particular, we found that PLEV tetrapeptide analogs with small C-terminal substituents, such as methoxy and ethoxy, displayed binding to both FGF14 and the Na$_v$1.6 CTD, whereas those with bulky C-terminal substituents, such as cycloalkanes, bound only to FGF14[31]. In a similar vein, we reason that replacing the small 3-methyl group on the phenyl ring of 7605 with the bulkier electron-withdrawing 3-carboxylic acid ethyl ester moiety of 1028 is what abrogates 1028's binding to the Na$_v$1.6 CTD and makes that region of the scaffold less lipophilic and more favorable for additional hydrogen bonding interactions, thereby causing it to interact only with FGF14.

To determine the functional activity of 1028, whole-cell voltage-clamp recordings were performed in HEK293 cells stably expressing the Na$_v$1.6 channel and FGF14 that were treated with either vehicle (DMSO) or 1 μM 1028 (Fig. 3f). The results of this single concentration activity screening are summarized in Supplementary Table S4. Notably, while 1 μM 1028 did not affect the peak I_{Na} density (Fig. 3g) or the voltage-dependence of activation (Fig. 3h) of currents elicited by these cells, the compound did induce a significant depolarizing shift in the voltage-dependence of steady-state inactivation (Fig. 3i). This effect of 1028 on the voltage-dependence of steady-state inactivation was dose-dependent, with a potency in the high nanomolar range (Fig. 3j). 1028's targeted effects on the voltage dependence of Na$_v$1.6 channel steady-state inactivation are expected to arise due to the compound's selective binding to FGF14. In our previous work with peptidomimetics, we have observed that peptidomimetic analogs that bind to both FGF14 and Na$_v$1.6 display a myriad of effects on Na$_v$1.6 channel function, including effects on Na$_v$1.6-mediated peak current density, the voltage-dependence of activation, and long-term inactivation[31,32]. Thus, for the three hits that bind to both FGF14 and the Na$_v$1.6 CTD (i.e., 5674, 7605,

https://doi.org/10.1038/s41467-024-55554-7

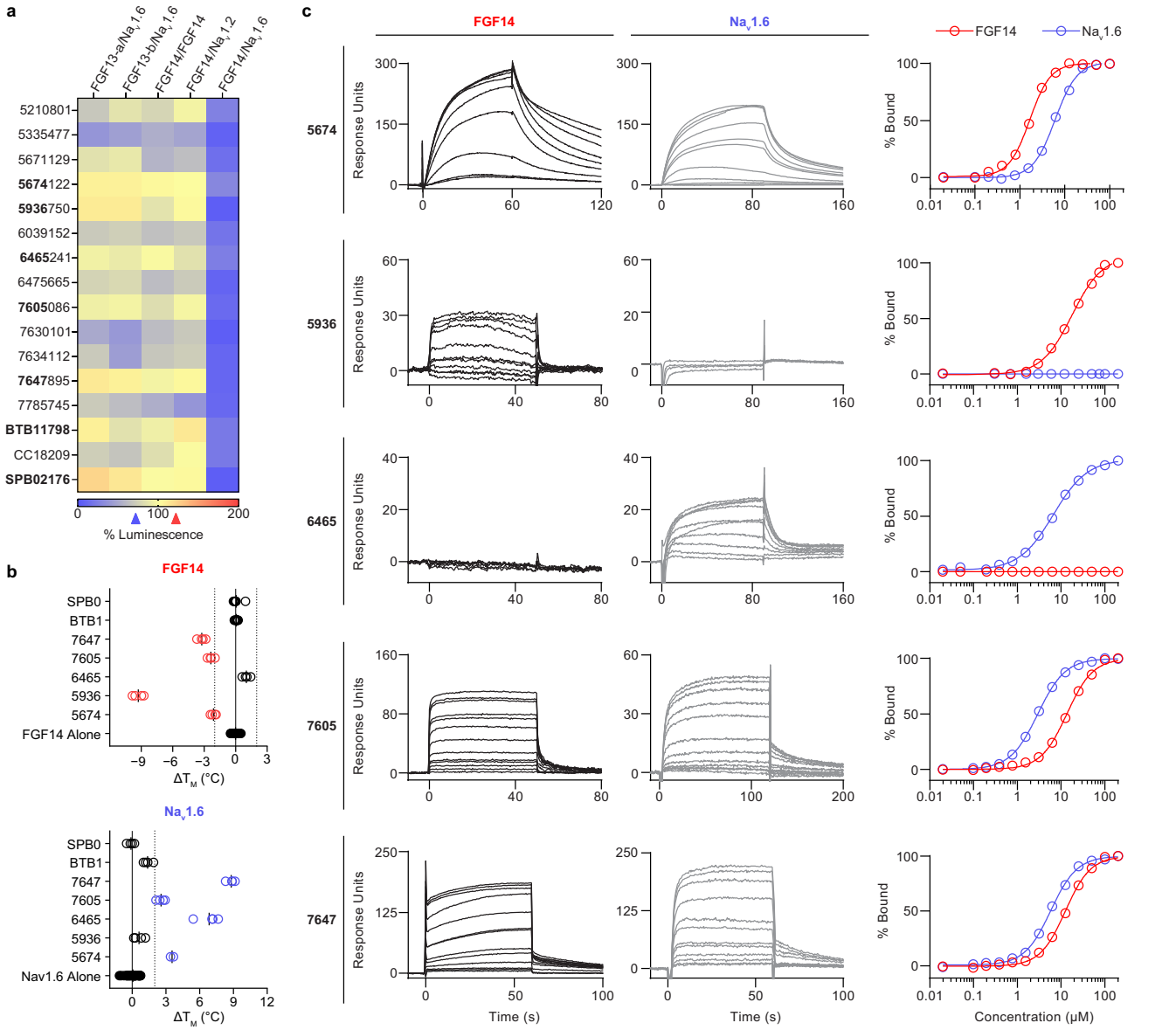

Fig. 2 | Characterization of selectivity and protein/ligand binding relationships. a The top 16 hits were repurchased and screened (50 μM) against the FGF13-1a/Na$_v$1.6, FGF13-1b/Na$_v$1.6, and FGF14/Na$_v$1.2 complexes, as well as the FGF14 dimer, using the LCA to assess compound selectivity toward the FGF14/Na$_v$1.6 complex. Compounds that modulated complex assembly by ≥ 25% were excluded from further studies, eliminating 9 at this stage. **b** Following selectivity screening, the top 7 compounds were screened for binding to purified FGF14 or Na$_v$1.6 CTD protein in 96-well plates (n = 4 per compound; 25 μM) using the fluorescence-based protein thermal shift (PTS) assay. Hits were defined as those compounds that resulted in a change in protein melting temperature (ΔT_M) of ≥ ± 2 °C compared to protein alone (n = 8/plate) and are highlighted as either red (hits against FGF14) or blue (hits against Na$_v$1.6). Individual replicates and the mean ΔT_M is shown for each condition. **c** The 5 remaining hits after the PTS assay were also quantitatively assessed for binding toward purified FGF14 and Na$_v$1.6 CTD protein using SPR. Binding sensorgrams are shown for FGF14 (left) and Na$_v$1.6 (middle), and normalized steady-state saturation plots (right) reveal differences in compound/protein binding affinities. Source data are provided as a Source Data file.

and 7647) we expect that these compounds would exert broader modulatory effects on Na$_v$1.6 channel function compared to the targeted regulation of steady-state inactivation conferred by 1028.

We next assessed the reproducibility of the effects of 1028 in a neuronal cell line. To do so, we performed voltage-clamp recordings of pharmacologically isolated Na$_v$1.6-mediated I_{Na} elicited by ND7-23 cells transfected with FGF14-GFP that were treated with either vehicle (DMSO) or 500 nM 1028 (Supplementary Fig. S4a). To pharmacologically isolate Na$_v$1.6-mediated I_{Na}, recordings were performed in the presence of a selective blocker of Na$_v$1.3 (100 nM ICA-121431) and Na$_v$1.7 (1 nM Protoxin-II), as Na$_v$1.3, Na$_v$1.6, and Na$_v$1.7 are the main Na$_v$ channel isoforms expressed in this neuronal cell line[35]. Consistent with the results of 1028 observed in the heterologous expression system, treatment of the aforementioned cells with 500 nM produced a marked shift in the voltage-dependence of inactivation of pharmacologically isolated Na$_v$1.6-mediated I_{Na} compared to vehicle treatment (Supplementary Fig. S4b). Also consistent with results observed in the heterologous expression system, 500 nM treatment neither affected the voltage-dependence of activation of the pharmacologically isolated Na$_v$1.6-mediated I_{Na} elicited by the ND7-23 cells transfected with FGF14-GFP (Supplementary Fig. S4c) nor the peak I_{Na} density (Supplementary Fig. S4d).

Effects of 1028 on MSN function

To assess the effects of 1028 on the cellular target of interest, whole-cell voltage-clamp recordings were performed in MSNs of the NAc in

https://doi.org/10.1038/s41467-024-55554-7

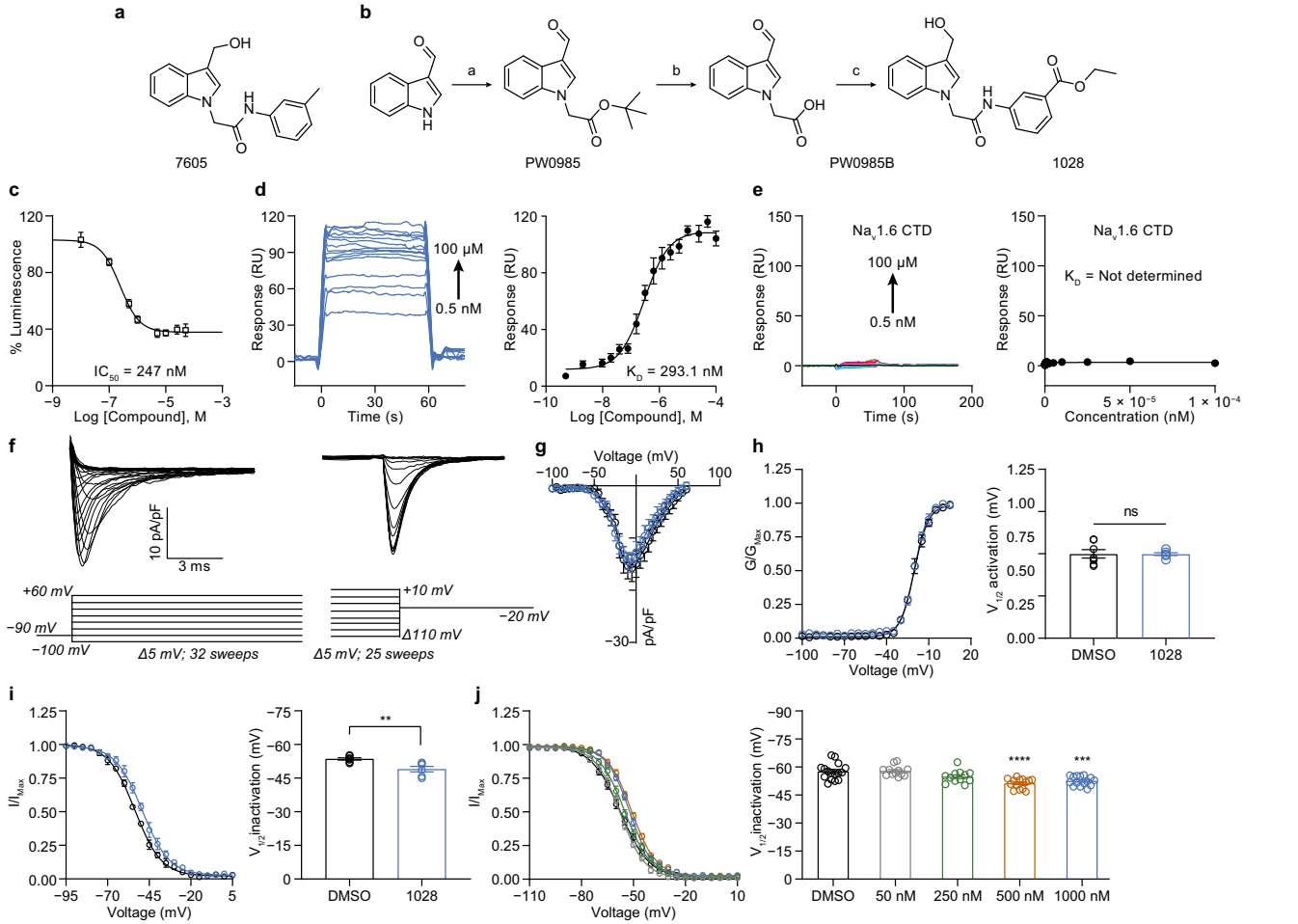

Fig. 3 | Lead optimization and functional evaluation. a Chemical structure of the top hit from the HTS, compound 7605. **b** Synthetic route of 1028. For detailed information regarding reagents and conditions, refer to the Supplementary Information. **c** Dose-dependent effects of 1028 on FGF14/$Na_v1.6$ complex assembly as determined using the LCA ($n = 32$ wells treated with vehicle; $n = 4$ wells/concentration of 1028). **d**, **e** Protein/ligand binding relationship of 1028 with FGF14 (**d**) and the $Na_v1.6$ CTD (**e**). SPR experiments were performed in triplicate. **f** Left: Representative traces of I_{Na} elicited by HEK293 cells stably expressing $Na_v1.6$ and FGF14 during the depicted activation protocol. Right: Representative traces of I_{Na} during the depicted inactivation protocol. **g**–**i** Characterization of the effects of 1 µM 1028 on the peak I_{Na} density (**g**; $n = 7$ for DMSO; $n = 6$ for 1028), voltage-dependence of activation (**h**; $n = 7$ for DMSO; $n = 6$ for 1028), and voltage-dependence of steady-state inactivation (**i**; $n = 7$ for DMSO; $n = 6$ for 1028) of currents elicited by HEK-$Na_v1.6$-FGF14-GFP cells. **j** Dose-dependent effects of 1028 on the voltage-dependence of steady-state inactivation of I_{Na} elicited by HEK-$Na_v1.6$-FGF14-GFP cells ($n = 16$ for DMSO; $n = 12$ for 50 nM 1028; $n = 12$ for 250 nM 1028; $n = 14$ for 500 nM 1028; $n = 15$ for 1000 nM 1028). Data are mean ± SEM. In (**g**–**i**), statistical significance was determined using a two-tailed Student's t test: ns, not significant; **, $p < 0.01$. In (**j**), significance was assessed using a one-way ANOVA with post hoc Dunnett's multiple comparisons test: ***, $p < 0.001$; ****, $p < 0.0001$. In (**i**), $p = 0.0044$. In (**j**), $p < 0.0001$ (DMSO versus 500 nM 1028) and $p = 0.0002$ (DMSO versus 1000 nM 1028). Source data are provided as a Source Data file.

slices from wild-type (WT) mice treated with vehicle (DMSO) or 1 µM 1028 (Fig. 4a). The concentration of DMSO used across slice electrophysiology was kept constant at 0.05%. To block K^+ current, the intracellular recording solution contained the non-selective K^+ channel blocker TEA-Cl (10 mM) and 4-aminopyridine (5 mM). To avoid space-clamp issues encountered when recording the I_{Na} of neurons in the slice preparation, we employed a previously described voltage-clamp protocol designed to mitigate space-clamp issues[36]. This protocol features, from the holding potential of −90 mV, a pre-pulse step to −35 mV, followed by a brief return to the holding potential (5 ms), followed by a test pulse. During the recovery interval at the holding potential, Na_v channels near the recording pipette have recovered from inactivation and are available to open upon subsequent stimulation, whereas those distal from the recording pipette remain inactivated due to the spatiotemporal spread of voltage from the pipette. Thus, only the Na_v channel function near to the pipette is recorded, allowing for well-clamp recordings of I_{Na} to be obtained. The results of this single concentration activity screening in voltage-clamp mode are summarized in Supplementary Tables S5 and S6. Consistent with the effects of 1028 in heterologous cells, 1 µM 1028 treatment neither affected the peak I_{Na} density (Fig. 4b) nor the voltage-dependence of activation (Fig. 4c) of I_{Na} elicited by MSNs, but induced a significant depolarizing shift in the voltage-dependence of steady-state inactivation (Fig. 4d) with high nanomolar potency as revealed by a dose-response analyses (Fig. 4e). However, 1 µM 1028 treatment of slices from knockout mice missing the *Fgf14* gene (*Fgf14*$^{-/-}$ mice; Fig. 4f) did not affect the peak I_{Na} density (Fig. 4g), the voltage-dependence of activation (Fig. 4h), or the voltage-dependence of steady-state inactivation (Fig. 4i) of I_{Na} elicited by MSNs. Importantly, these *Fgf14*$^{-/-}$ mice feature a global knockout of *Fgf14* and have previously been characterized[37] and lack FGF14 expression in the NAc (Supplementary Fig. S5). These results suggest that the mechanism of action (MOA) of 1028 is dependent upon the presence of FGF14 protein. Further supporting the conclusion that 1028's effects on the inactivation of I_{Na} of MSNs are dependent upon the presence of FGF14, we performed a 2-way ANOVA (drug x genotype), and the interaction effect was found to have a p-value of 0.0009.

https://doi.org/10.1038/s41467-024-55554-7

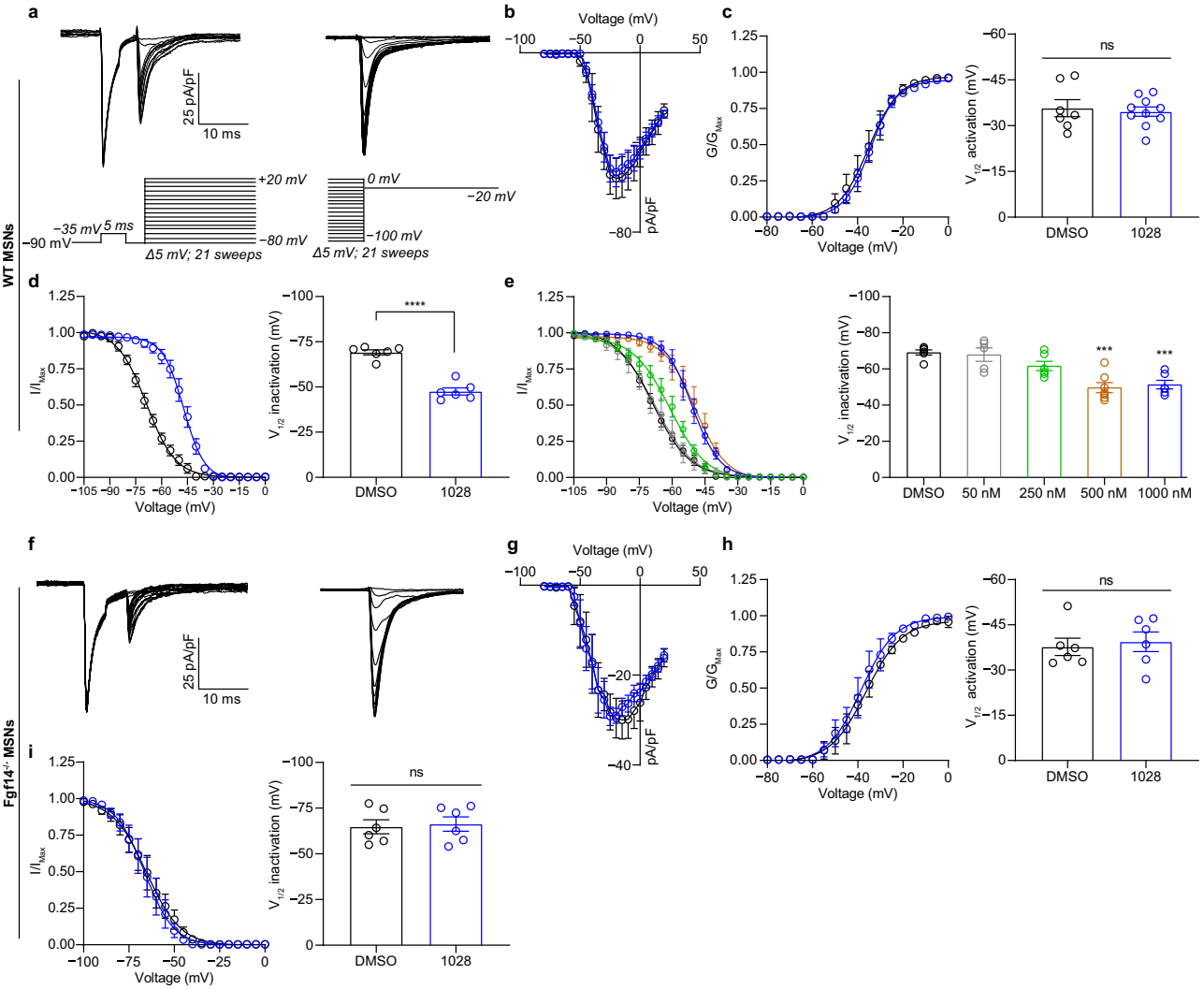

Fig. 4 | Effects of 1028 on the I_{Na} of MSNs. a Left: Representative trace of I_{Na} elicited by MSN of the NAc in response to the depicted activation protocol. Right: Representative trace of I_{Na} elicited by MSN of the NAc in response to the depicted inactivation protocol. **b**–**d** Effects of 1 μM 1028 treatment on the peak I_{Na} density (**b**; $n = 7$ for DMSO; $n = 10$ for 1028), voltage-dependence of activation (**c**; $n = 7$ for DMSO; $n = 10$ for 1028), and voltage-dependence of steady-state inactivation (**d**; $n = 6$ for DMSO; $n = 6$ for 1028) of I_{Na} elicited by MSNs of the NAc. **e** Dose-dependent effects of 1028 on the voltage-dependence of steady-state inactivation of I_{Na} elicited by MSNs of the NAc ($n = 6$ for DMSO; $n = 5$ for 50 nM 1028; $n = 6$ for 250 nM 1028; $n = 7$ for 500 nM 1028; $n = 6$ for 1000 nM). **f** Representative traces of I_{Na} elicited by MSNs of the NAc in a slice from a *Fgf14*$^{-/-}$ mice in response to the voltage-clamp protocols shown in (**a**). **g**–**i** Effects of 1 μM 1028 treatment on the peak I_{Na} density (**g**; $n = 6$ for DMSO; $n = 6$ for 1028), voltage-dependence of activation (**h**; $n = 6$ for DMSO; $n = 6$ for 1028), and voltage-dependence of steady-state inactivation (**i**; $n = 6$ for DMSO; $n = 6$ for 1028) of I_{Na} elicited by MSNs of the NAc in slices from *Fgf14*$^{-/-}$ mice. Data are mean ± SEM. In (**b**–**d**) and (**g**–**i**), significance was assessed using a two-tailed Student's *t* test: ns, not significant; ****, $p < 0.0001$ (Slices from $N = 3$ mice/group). In (**e**) significance was assessed using a one-way ANOVA with post hoc Dunnett's multiple comparisons test: ***, $p < 0.001$; ****, $p < 0.0001$ (Slices from $N = 3$ mice/group). In (**d**) $p < 0.0001$. In (**e**) $p < 0.0001$ (DMSO versus 500 nM 1028) and $p = 0.0003$ (DMSO versus 1000 nM 1028). Source data are provided as a Source Data file.

To ensure that the currents measured were Na_v channel mediated, we performed a separate set of these voltage-clamp experiments before and after 1 μM TTX application. As shown in Supplementary Fig. S6, 1 μM TTX application almost entirely blocks the observed currents, demonstrating that, indeed, the inward currents were mediated by Na_v channels. While these voltage-clamp experiments in MSNs recapitulate the effects of 1028 observed in heterologous cells, one notable observation is that the effect size of 1028 in terms of depolarizing the voltage-dependence of inactivation of I_{Na} is markedly larger in MSNs than in the heterologous expression system. While the precise mechanism for this differential effect size is unresolved, there are a few possible explanations. Firstly, in the HEK293 cell line, $Na_v1.6$ and FGF14 are overexpressed, whereas in MSNs, the proteins are expressed at physiological levels. Thus, one possibility is that the difference in effect size is a result of differences in the overall expression levels of FGF14 and $Na_v1.6$ in the two systems, or due to a potential difference in the stoichiometry of the expression in the heterologous system versus the slice preparation. Secondly, additional Na_v channel auxiliary proteins (e.g., FGF13) and Na_v channel subunits (beta-IV) are expressed in MSNs versus in the heterologous system. Thus, it is possible that the presence of these additional proteins within the $Na_v1.6$ channel interactome influences the functional activity of 1028 against its target FGF14/$Na_v1.6$. These differences in the heterologous expression system versus the slice preparation, in tandem with differences related to how FGF14 and $Na_v1.6$ might be post-translationally modified in the two systems, should be considered when comparing the effect size of 1028 on the voltage-dependence of inactivation in the HEK293 cell line versus the slice preparation.

We next investigated if 1028's effects on the voltage-dependence of steady-state inactivation of I_{Na} of NAc MSNs would confer changes in

https://doi.org/10.1038/s41467-024-55554-7

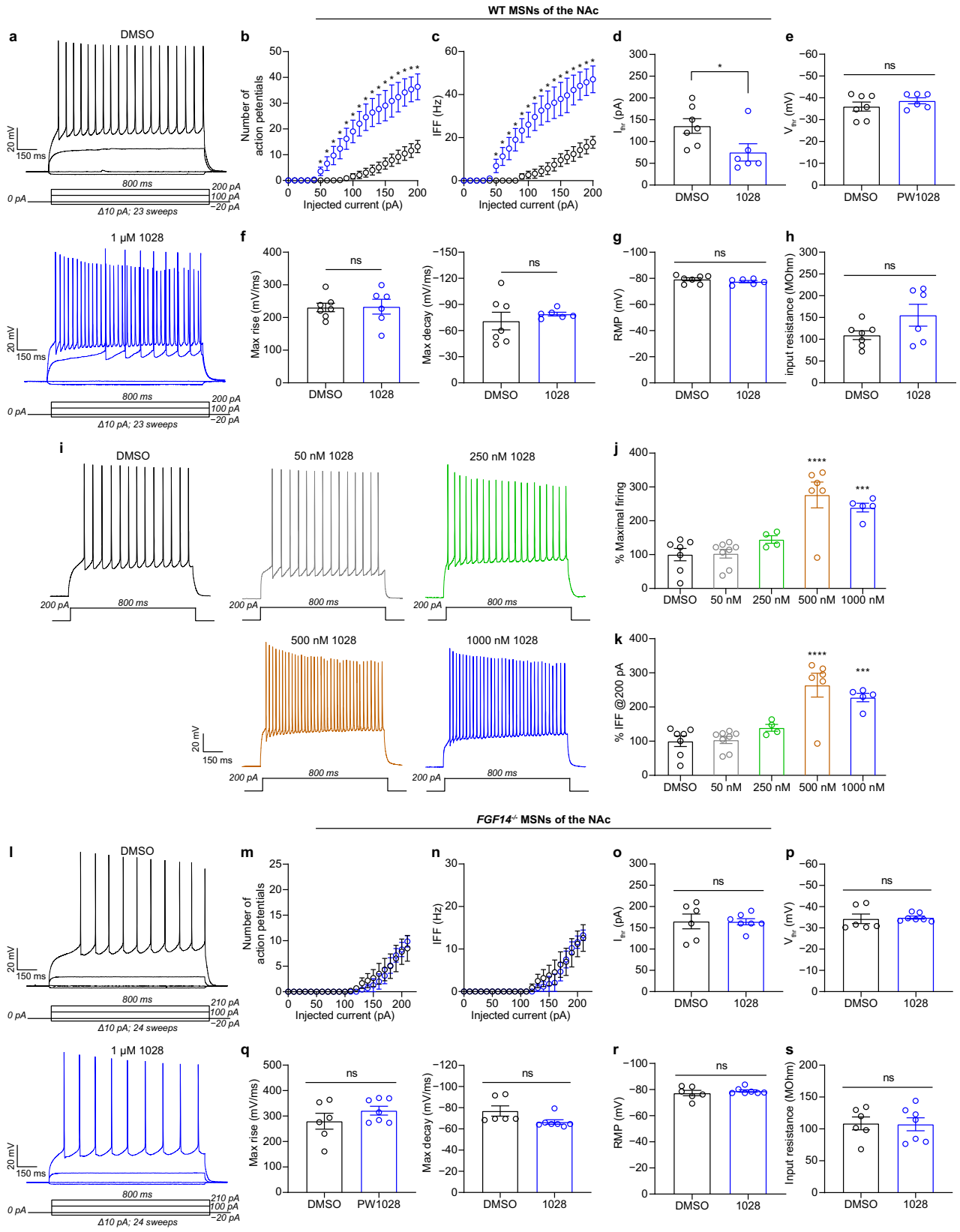

the intrinsic excitability of these cells. To that end, whole-cell current-clamp recordings were performed in slices from WT mice treated with vehicle (DMSO) or 1 μM of 1028 (Fig. 5a). The results of this single concentration activity screening in current-clamp mode are summarized in Supplementary Tables S7, S8. Consistent with the recordings above, treatment of WT slices with 1 μM of 1028 resulted in increased maximal firing (Fig. 5b) and instantaneous firing frequency (IFF; Fig. 5c) across a range of injected current stimuli compared to vehicle treatment. In addition, MSNs treated with 1 μM 1028 displayed a lower current threshold for action potential initiation compared to vehicle-treated MSNs (Fig. 5d). However, other properties including the voltage threshold for action potential initiation (Fig. 5e), action potential

Fig. 5 | 1028 increases the excitability of MSNs of the NAc in a FGF14 dependent manner. a, **l** Traces of evoked APs of MSNs in slices from WT mice (**a**) or *Fgf14*$^{-/-}$ mice (**l**) treated with DMSO (black) or 1 μM 1028 (blue). **b**, **c**, **m**, **n** Number of evoked APs as a function of injected current (**b**, **m**) and IFF as a function of injected current (**c**, **n**) in the indicated experiments group (WT mice: $n = 7$ for DMSO, $n = 6$ for 1028; *Fgf14*$^{-/-}$ mice: $n = 6$ for DMSO; $n = 7$ for 1028). **d**–**h**, **o**–**s** Comparison of the current threshold (**d**, **o**), voltage threshold (**e**, **p**), AP kinetics (**f**, **q**), resting membrane potential (**g**, **r**), and input resistance (**h**, **s**) in the indicated experimental groups (WT mice: $n = 7$ for DMSO, $n = 6$ for 1028; *Fgf14*$^{-/-}$ mice: $n = 6$ for DMSO; $n = 7$ for 1028). **i** Traces of evoked APs of MSNs in the indicated condition. **j**, **k** Dose-response analyses of the effects of 1028 on maximal firing (**j**; $n = 7$ for DMSO; $n = 8$ for 50 nM 1028; $n = 4$ for 250 nM 1028; $n = 6$ for 500 nM 1028; $n = 5$ for 1000 nM 1028) and IFF (**k**; $n = 7$ for DMSO; $n = 8$ for 50 nM 1028; $n = 4$ for 250 nM 1028; $n = 6$ for 500 nM 1028; $n = 5$ for 1000 nM 1028) of MSNs. Data are mean ± SEM. In (**b**, **c**) * denotes current steps at which the number of action potentials or IFF is significantly greater (p is at least < 0.05; Student's t test) for MSNs treated with 1028 compared to vehicles. In (**d**–**h**) and (**o**–**s**), significance was assessed using a two-tailed Student's t test: ns, not significant; *, $p < 0.05$ (Slices from $N = 3$ mice/group). In (**j**, **k**) significance was assessed using a one-way ANOVA with post hoc Dunnett's multiple comparisons test: ***, $p < 0.001$; ****, $p < 0.0001$ (Slices from $N = 3$ mice/group). For exact p-values, refer to Supplementary Tables S7 and S8. Source data are provided as a Source Data file.

kinetics (Fig. 5f), resting membrane potential (Fig. 5g), and input resistance (Fig. 5h) were unaffected by the treatment. Notably, the voltage threshold for action potential initiation and the kinetics of the upstroke of the action potential is primarily regulated by the kinetics and voltage-dependence of activation of Na_v channels[38,39]. Thus, the lack of effects of 1028 on these parameters is consistent with 1028's targeted effects on the voltage dependence of steady-state inactivation. Furthermore, the kinetics of the downstroke of the action potential, the resting membrane potential, and the input resistance are primarily regulated by a variety of calcium and potassium channels[40–42]. Thus, the lack of effects of 1028 on these parameters argues against 1028 having modulatory effects on off-target ion channels.

We further performed a dose-response to characterize the potency with which 1028 increases the intrinsic excitability of MSNs (Fig. 5i). The dose dependency of 1028's effects on maximal firing (Fig. 5j) and IFF (Fig. 5k) was similar to 1028's dose dependency in terms of depolarizing the voltage-dependence of steady-state inactivation of I_{Na} of MSNs, suggesting that the effect on I_{Na} and excitability induced by 1028 were causally related. Importantly, while 1028 increased MSN excitability in slices from WT mice with potency in the high nanomolar range, treatment of slices from *Fgf14*$^{-/-}$ mice with 1 μM 1028 did not induce any changes in active (Fig. 5l–q) or passive (Fig. 5r, s) electrical properties of MSNs of the NAc, demonstrating that 1028's modulatory effects on MSNs depend upon the presence of FGF14.

Mechanism of action and selectivity of 1028

Next, we sought to elucidate the molecular mechanisms contributing to the observed modulation of neuronal activity induced by 1028. To that end, we developed an AlphaFold2 (AF2) model of FGF14 and then performed molecular docking of 1028 with the newly developed AF2 model of FGF14. These molecular docking studies predicted that the hydroxyl group and backbone ring structure of 1028 had a hydrogen bond and Pi cation interaction, respectively, with the R117 residue of FGF14 (Fig. 6a). Notably, AF2 modeling of the FGF14/$Na_v1.6$ PPI interface predicted an intermolecular interaction between $FGF14^{R117}$ and $Na_v1.6^{D1846}$, the latter of which putatively forms a salt bridge with $Na_v1.6^{R1866}$ (Fig. 6b). On account of these putative interactions of compound 1028 with $FGF14^{R117}$ and of $FGF14^{R117}$ with the $Na_v1.6^{D1846:R1866}$ salt bridge, we hypothesized that compound 1028 might affect FGF14/$Na_v1.6$ complex assembly via modulation of this intermolecular interaction. To that end, we repeated LCA experiments in conditions in which $FGF14^{R117}$ or the interaction site of $FGF14^{R117}$ on the CTD (i.e., the $Na_v1.6^{D1846:R1866}$ salt bridge) were mutated to alanine. In these experiments, the LCA signal was normalized to each condition per plate control wells treated with DMSO. For example, the average luminescence was calculated for wells treated with DMSO in the $FGF14^{R117A}$/$Na_v1.6$ condition, and then all wells in the $FGF14^{R117A}$/$Na_v1.6$ condition were normalized to this value. This method of normalization was then employed for the other mutant conditions tested. We observed that LCA experiments in the presence of $FGF14^{R117A}$ almost entirely prevented compound 1028 from conferring modulatory effects on complex assembly (Fig. 6c), as did mutating the interaction site of $FGF14^{R117}$ on the $Na_v1.6$ channel (Fig. 6d). Further supporting our LCA results, compound 1028 showed no detectable binding to purified $FGF14^{R117A}$ protein in SPR studies (Fig. 6e), lending further credence to the salience of the compound 1028/$FGF14^{R117}$ interaction in conferring the compound's effects on complex assembly. To determine whether the transiently transfected HEK293 cells expressed the LCA constructs to a reasonable degree, we performed immunofluorescence analysis on the transfected cells followed by confocal imaging. The average fluorescence intensity profile measurement of the $FGF14^{WT}$/$Na_v1.6^{WT}$ condition shows a similar pattern of mean intensity profiles between red and green channels compared to the mutant conditions, indicating comparable colocalization between CLuc- and NLuc-tagged proteins across conditions (Supplementary Fig. S7). In addition, to compare the extent to which the FGF14/$Na_v1.6$ complex still forms in the presence of the mutations assayed, we compared the luminescence signal observed in the mutant conditions to the luminescence signal observed in the $FGF14^{WT}$/$Na_v1.6^{WT}$ condition (Supplementary Fig. S8). We observed that while the mutations caused a reduction in complex assembly, there remained a robust luminescence signal compared to untransfected cells (Supplementary Fig. S8), indicating that appreciable complex assembly still occurred in the mutant conditions. What this indicates is that while complex assembly is reduced due to the absence of the hot spot residue $FGF14^{R117}$ or its interaction site on the $Na_v1.6$ CTD, contacts remain between other hot spot residues of FGF14 (e.g., $FGF14^{K74}$, $FGF14^{Y158}$, $FGF14^{V160}$) and their corresponding interaction sites on the CTD[43], which still allows for the complex to form, albeit in a reduced capacity. Given this, the observation that 1028 does not produce effects in the mutant conditions assayed indicates that 1028's effects are targeted toward the $FGF14^{R117}Na_v1.6^{D1846:R1866}$ interaction and don't affect the intermolecular interactions that remain in the presence of mutating $FGF14^{R117}$ or its interaction site on the $Na_v1.6$ CTD.

We next sought to determine the mechanism by which 1028 causes a depolarizing shift in the voltage dependence of steady-state inactivation of I_{Na}. Notably, previous structural studies have demonstrated that interactions of intracellular fibroblast growth factors (iFGF; also referred to as fibroblast growth factor homologous factor, FHF) with the CTDs of Na_v channels results in disruption of the intramolecular interaction between the IQ domain and the EF-hand domain of the CTD[44], the latter of which has the ability to interact with the III-IV linker[45], which causes changes in Na_v channel inactivation[46]. This led to the hypothesis that the effect of 1028 on $Na_v1.6$ channel steady-state inactivation was mediated by modulating this intramolecular interaction. To test this hypothesis, we repeated voltage-clamp experiments in HEK293 cells that were transiently transfected with wild-type or mutant $Na_v1.6$ cDNA and wild-type FGF14-GFP cDNA.

Consistent with the effects of 1028 in the HEK-$Na_v1.6$-FGF14-GFP stable cell line, 1 μM 1028 caused a depolarizing shift in the voltage-dependence of steady-state inactivation of I_{Na} in HEK293 cells transiently transfected with $Na_v1.6^{WT}$ and FGF14 (Fig. 6f). Because the

https://doi.org/10.1038/s41467-024-55554-7

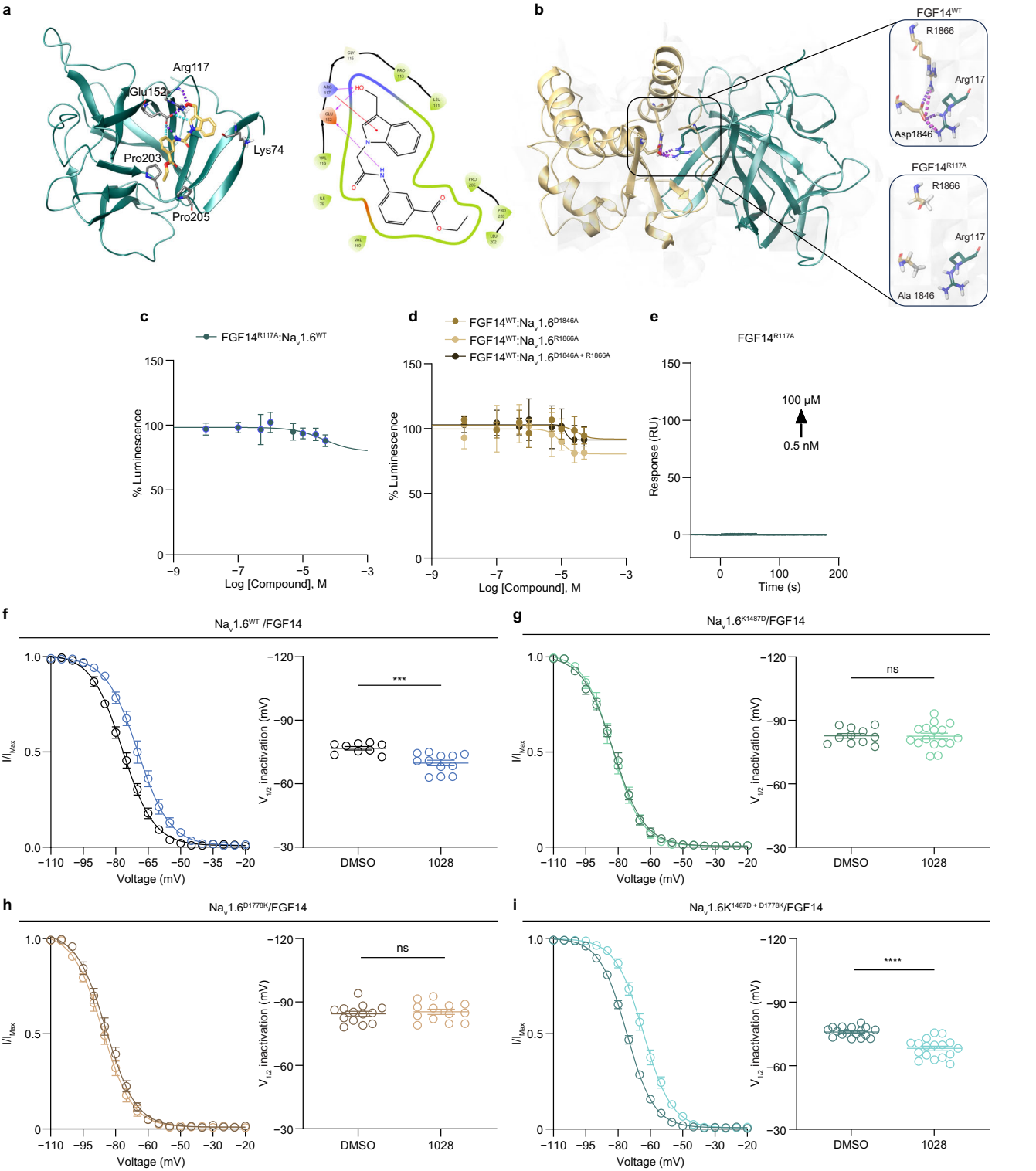

Fig. 6 | Molecular mechanism of 1028's effects on FGF14/$Na_v1.6$ complex assembly and $Na_v1.6$ channel inactivation. a Left: Ribbon representation of 1028 docking with the AF2 model of FGF14. Right: 2D interaction map derived from the molecular docking of 1028 with the AF2 model of FGF14 highlighting key interactions of 1028 with FGF14. **b** AF2 modeling of the FGF14/$Na_v1.6$ PPI interface showing the intermolecular interaction between $FGF14^{R117}$ and the $Na_v1.6^{D1846:R1866}$ salt bridge. **c**, **d** LCA studies of 1028 in the presence of the indicated FGF14 (**c**) and $Na_v1.6$ CTD (**d**) mutants ($n = 4$/concentration). **e** Protein:ligand binding study of $FGF14^{R117A}$/1028 using SPR. SPR experiments were performed in triplicate. **f** Effects of 1 µM 1028 on the voltage-dependence of steady-state inactivation when tested in HEK293 cells transiently expressing WT $Na_v1.6$ and WT FGF14 ($n = 9$ for DMSO; $n = 12$ for 1028). **g**, **h** Lack of effects of 1 µM 1028 on the voltage-dependence of steady-state inactivation when tested in HEK293 cells transiently expressing $Na_v1.6^{K1487D}$ and FGF14 (**g**; $n = 11$ for DMSO; $n = 16$ for 1028) or $Na_v1.6^{D1778K}$ and FGF14 (**h**; $n = 13$ for DMSO; $n = 13$ for 1028). **i** Effects of 1 µM 1028 on the voltage-dependence of steady-state inactivation when tested in HEK293 cells transiently expressing the $Na_v1.6^{K1487D+D1778K}$ double mutant and FGF14 ($n = 17$ for DMSO; $n = 17$ for 1028). Data are mean ± SEM. In (**f**, **g**, **h**, and **i**) significance was assessed using a two-tailed Student's *t* test: ns, not significant, ***, $p < 0.001$; ****, $p < 0.0001$ (Cells from $N = 3$ independent transfections/group). In (**f**) $p = 0.0005$. In (**i**) $p < 0.0001$. Source data are provided as a Source Data file.

putative interaction between the III-IV linker and CTD for the $Na_v1.6$ channel is formed between $Na_v1.6^{K1487}$ and $Na_v1.6^{D1778K}$ [46], we introduced mutations that alter and destabilize the charge ratio of the interaction ($Na_v1.6^{K1487D}$ and $Na_v1.6^{D1778K}$), as shown in previous reports for the $Na_v1.5$ channel[46]. Consistent with 1028's effects on inactivation requiring an intact interaction between the III-IV linker and CTD, 1 μM 1028 treatment of HEK293 cells transiently transfected with either $Na_v1.6^{K1487D}$ or $Na_v1.6^{D1778K}$ in combination with FGF14 did not cause any effect on the voltage-dependence of steady-state inactivation (Fig. 6g, h). Gade et al.[46] previously showed that the charge ratio of the interaction between III-IV linker and CTD of the $Na_v1.5$ channel was important for stabilizing the interaction, as a double $Na_v1.5$ channel mutant that restored the charge ratio of the interaction ($Na_v1.5^{K1493E+E1784K}$) restored the voltage-dependence of steady-state inactivation of the $Na_v1.5$ channel back to a level comparable to the $Na_v1.5^{WT}$ condition. Thus, we next tested if restoration of the charge ratio of the intramolecular interaction between the III-IV linker and CTD of the $Na_v1.6$ channel in the presence of FGF14 would restore 1028's effects on the voltage dependence of steady-state inactivation. Consistent with 1028's effects on $Na_v1.6$ channel steady-state inactivation being dependent on the charge ratio of the intramolecular interaction between the III-IV linker and CTD, in HEK293 cells transiently transfected with the $Na_v1.6^{K1487D+D1778K}$ double mutant along with FGF14, 1 μM 1028 retained its effects on the voltage-dependence of steady-state inactivation in these cells (Fig. 6i). Collectively, these data provide evidence that 1028 causes a depolarizing shift in the voltage-dependence of steady-state inactivation of I_{Na} by modulating the interaction of the III-IV linker with the CTD. To ensure that $Na_v1.6$ channel levels were consistent across the mutant conditions and that the mutations introduced did not affect protein expression, we compared the I_{Max} among the mutant conditions, and no significant differences in this parameter were observed (Supplementary Table S9), indicating that channel expression levels were not affected by the mutations.

We next assessed the selectivity of 1028 for the $Na_v1.6$/FGF14 macromolecular complex. Notably, $Na_v1.1$ and $Na_v1.2$ channels, along with the $Na_v1.6$ channel, represent the primary Na_v channel isoforms expressed in the brain[47], and FGF14 interacts with the CTDs of all three isoforms giving rise to unique regulatory effects on the different Na_v channel isoforms[8,29]. Thus, to assess selectivity for the $Na_v1.6$/FGF14 macromolecular complex, we employed whole-cell voltage-clamp recordings in HEK293 cells stably expressing the $Na_v1.1$ channel and FGF14 (Supplementary Fig. S9a) or $Na_v1.2$ channel and FGF14 (Supplementary Fig. S9e). 1 μM treatment with 1028 had no effect on the voltage-dependence of steady-state inactivation of I_{Na} in HEK293 cells expressing $Na_v1.1$ and FGF14 (Supplementary Fig. S9b) or $Na_v1.2$ and FGF14 (Supplementary Fig. S9f). In addition, 1 μM 1028 treatment did not alter the peak I_{Na} density (Supplementary Fig. S9c, g)) or the voltage-dependence of activation (Supplementary Fig. S9d, h)) in either cell line, collectively indicating selective regulation of the $Na_v1.6$ channel macromolecular complex. Lending potential insights into the mechanism by which 1028 is selective for the FGF14/$Na_v1.6$ macromolecular complex, AF2 modeling of the FGF14/$Na_v1.6$ PPI interface revealed that when FGF14 is in complex with $Na_v1.6$, $FGF14^{R117}$ is accessible to 1028 (Supplementary Fig. S10a); however, when FGF14 is in complex with $Na_v1.1$ or $Na_v1.2$, $FGF14^{R117}$ is not accessible to 1028 (Supplementary Fig. S10b, c).

We next tested if compound 1028's interaction with $FGF14^{R117}$ was required to produce its effect on the intrinsic excitability of MSNs of the NAc. To test this, *Fgf14*$^{-/-}$ mice were stereotaxically injected with either AAV-GFP, AAV-FGF14-GFP, or AAV-$FGF14^{R117A}$-GFP into the NAc. To confirm the expression of FGF14-GFP and $FGF14^{R117A}$-GFP, confocal images were taken from tissue slices 3 weeks after injection. The analysis of the maximum fluorescent intensity of the GFP signals shows no significant difference between FGF14-GFP and $FGF14^{R117A}$-GFP (Supplementary Fig. S11), indicating that the expression levels of wild-type and mutant FGF14 protein via viral vectors were comparable. Three weeks after stereotaxic surgery, current-clamp recordings were performed in slices from mice in the three experimental conditions (Fig. 7a). Consistent with Fig. 5l-n, 1 μM compound 1028 treatment had no effect when tested in MSNs in slices from *Fgf14*$^{-/-}$ mice previously injected with AAV-GFP (Fig. 7b). However, reintroducing WT FGF14 into the NAc of *Fgf14*$^{-/-}$ mice restored 1028's effect on the intrinsic excitability of MSNs, as evidenced by MSNs in slices from *Fgf14*$^{-/-}$ mice previously injected with AAV-FGF14-GFP and treated with 1 μM of compound 1028 exhibiting increased maximal firing and IFF compared to vehicle-treated slices (Fig. 7c). Notably, in line with 1028's interaction with $FGF14^{R117}$ being required for the compound's potentiation of MSN firing, 1028 had no effect when tested in slices from *Fgf14*$^{-/-}$ mice previously injected with AAV-$FGF14^{R117A}$-GFP (Fig. 7d). Collectively, these results provide mechanistic evidence that the interaction of 1028 with $FGF14^{R117}$ is necessary for driving its functional effects on $Na_v1.6$ channel inactivation and MSN excitability.

1028 Increases firing rates of accumbal neurons in vivo and maintains behavioral motivation preferentially during unmotivated states

Given compound 1028's promising in vitro and ex vivo activity, we next determined its in vivo pharmacokinetic profile. The pharmacokinetic profile of compound 1028 was evaluated in rats after a single dose of 10 mg/kg administered intraperitoneally (IP), and the results are summarized in(Supplementary Table S10). Compound 1028 had acceptable plasma exposure ($AUC_{0\text{-}inf}$ = 941.7 ± 152.5 h*ng/mL) and maximum serum concentration (C_{max} = 980.1 ± 69.9 ng/mL) following IP administration. In addition, compound 1028 displayed an acceptable volume of plasma distribution (V_z = 7.56 ± 1.14 L/kg) and plasma clearance (CL = 11.1 ± 1.55 L/h/kg). Additionally, compound 1028 (10 mg/kg, IP) was further evaluated in rats for brain permeability after a single injection, and the concentration of compound 1028 in the brain and plasma was measured at 0.5 h and 1 h (Supplementary Table S11). We observed a modest level of compound 1028 in the brain at 0.5 h (110.1 ± 11.1 ng/g) and 1 h (115.9 ± 35.3 ng/g) after the administration, with a brain/plasma ratio of 0.20 ± 0.01 at 0.5 h and 0.23 ± 0.04 at 1 h.

Considering the blood-brain barrier penetrance of compound 1028, we next investigated if the observed ex vivo effects of compound 1028 could be recapitulated in vivo. To do so, we used in vivo single-unit recordings to measure the spontaneous firing rates of NAc neurons, ~ 95% of which are MSNs[13], after IP injection of vehicle (5% DMSO, 15% solutol, 80% saline) followed by compound 1028 (5 mg/kg, IP; Fig. 8a–c). We observed that 36% (12 out of 33 neurons) of the recorded NAc cells displayed a significant increase (Z-score > 2.58) in firing rates following 1028 administration, compared to 6% following vehicle injection (2 out of 33 neurons, Fisher Exact test, p = 0.0053, Fig. 8d, e). While 36% of NAc neurons showed reduced activity after vehicle injection and increased firing rates following 1028 injection, the remaining 64% of neurons were insensitive to either vehicle or 1028 (Fig. 8f, right), suggesting that 1028 preferentially affects NAc neurons exhibiting reduced activity throughout the session. To control for changes in neuronal firing rates, we normalized cell activity after compound injection to a second baseline interval of 3 min, as shown in Fig. 8c. Because increased NAc activity has been associated with higher motivation to seek rewards[48,49], we used a cued sucrose-seeking protocol to test the effects of 1028 during both food restricted and food satiated conditions in rats (Fig. 8g, see "Methods"). During the baseline for the food-restricted condition, there was a significant main effect of time as it relates to changes in lever presses per minute early in the session (first four cues) compared to late in the session (last four cues) ($F_{(1,13)}$ = 18.27; p = 0.0009). A Sidak's multiple comparisons tests demonstrated that groups treated with either vehicle or 1028 pressed

https://doi.org/10.1038/s41467-024-55554-7

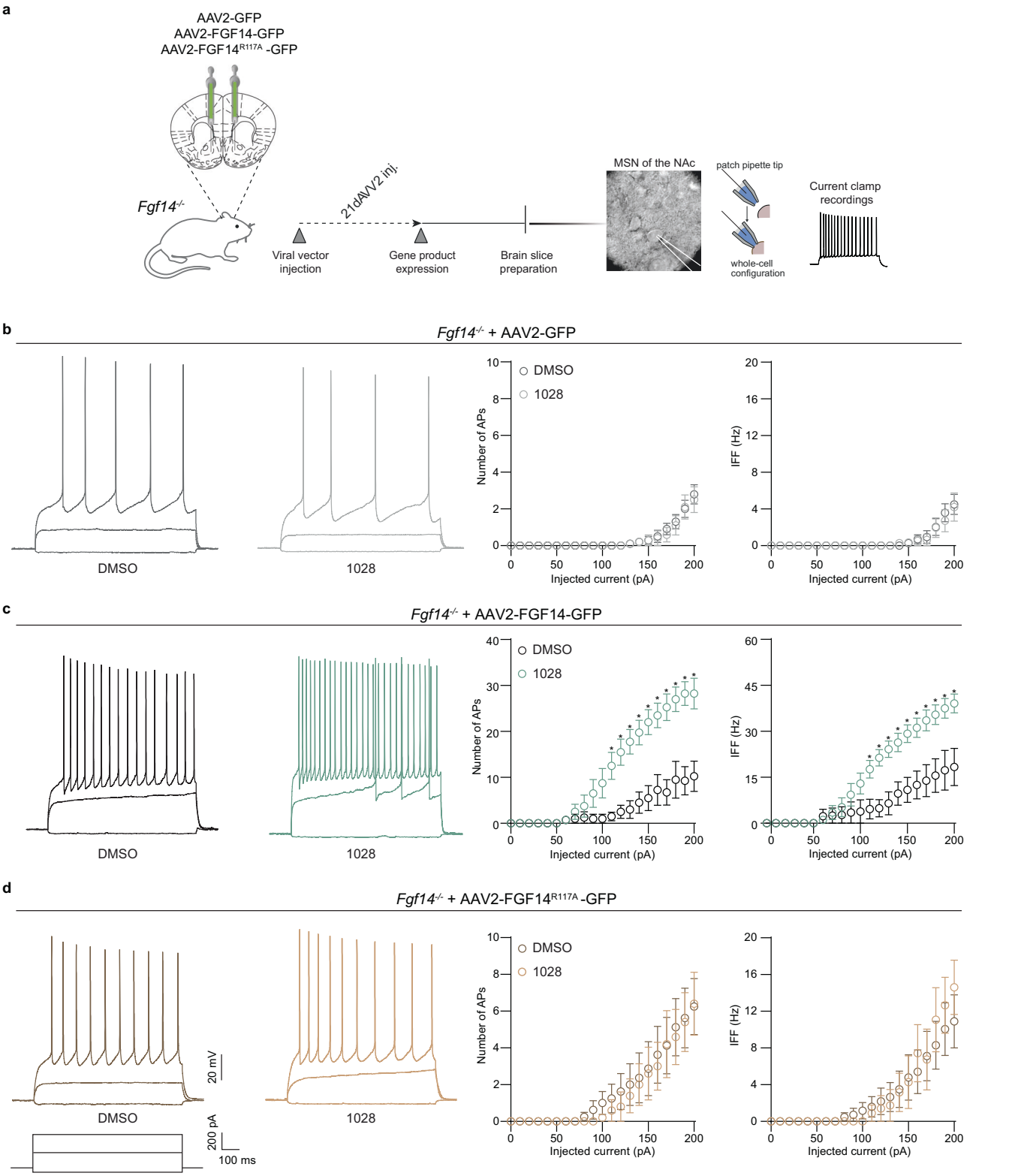

Fig. 7 | 1028 potentiates MSN excitability through a FGF14^{R117} dependent mechanism. a Experimental timeline. **b**–**d** Effects of 1 μM 1028 on the maximal firing and IFF of MSNs of the NAc when tested in slices from *Fgf14*$^{-/-}$ mice stereotaxically injected with AAV-GFP (**b**; $n = 10$ for DMSO; $n = 10$ for 1028), AAV-FGF14-GFP (**c**; $n = 4$ for DMSO; $n = 4$ for 1028), or AAV-FGF14^{R117A}-GFP (**d**; $n = 8$ for DMSO; $n = 5$ for 1028). Data are mean ± SEM. In input/output plots, * denotes current steps at which the number of action potentials or IFF is significantly higher (p is at least < 0.05; two-tailed Student's t test) in MSNs treated with 1028 compared to vehicle (Slices from $N = 2$–3 mice/group). In c for number of APs as a function of time, $p = 0.0122$ (110 pA), $p = 0.0068$ (120 pA), $p = 0.0042$ (130 pA), $p = 0.0052$ (140 pA), $p = 0.0053$ (150 pA), $p = 0.0090$ (160 pA), $p = 0.0037$ (170 pA), $p = 0.0110$ (180 pA), $p = 0.0032$ (190 pA), $p = 0.0085$ (200 pA). In c for IFF as a function of time, $p = 0.0228$ (110 pA), $p = 0.0057$ (120 pA), $p = 0.0085$ (130 pA), $p = 0.0143$ (140 pA), $p = 0.0105$ (150 pA), $p = 0.0150$ (160 pA), $p = 0.0196$ (170 pA), $p = 0.0201$ (180 pA), $p = 0.0308$ (190 pA), $p = 0.0229$ (200 pA). Source data are provided as a Source Data file. Illustrations shown in a were designed and provided by Research Creative.

https://doi.org/10.1038/s41467-024-55554-7

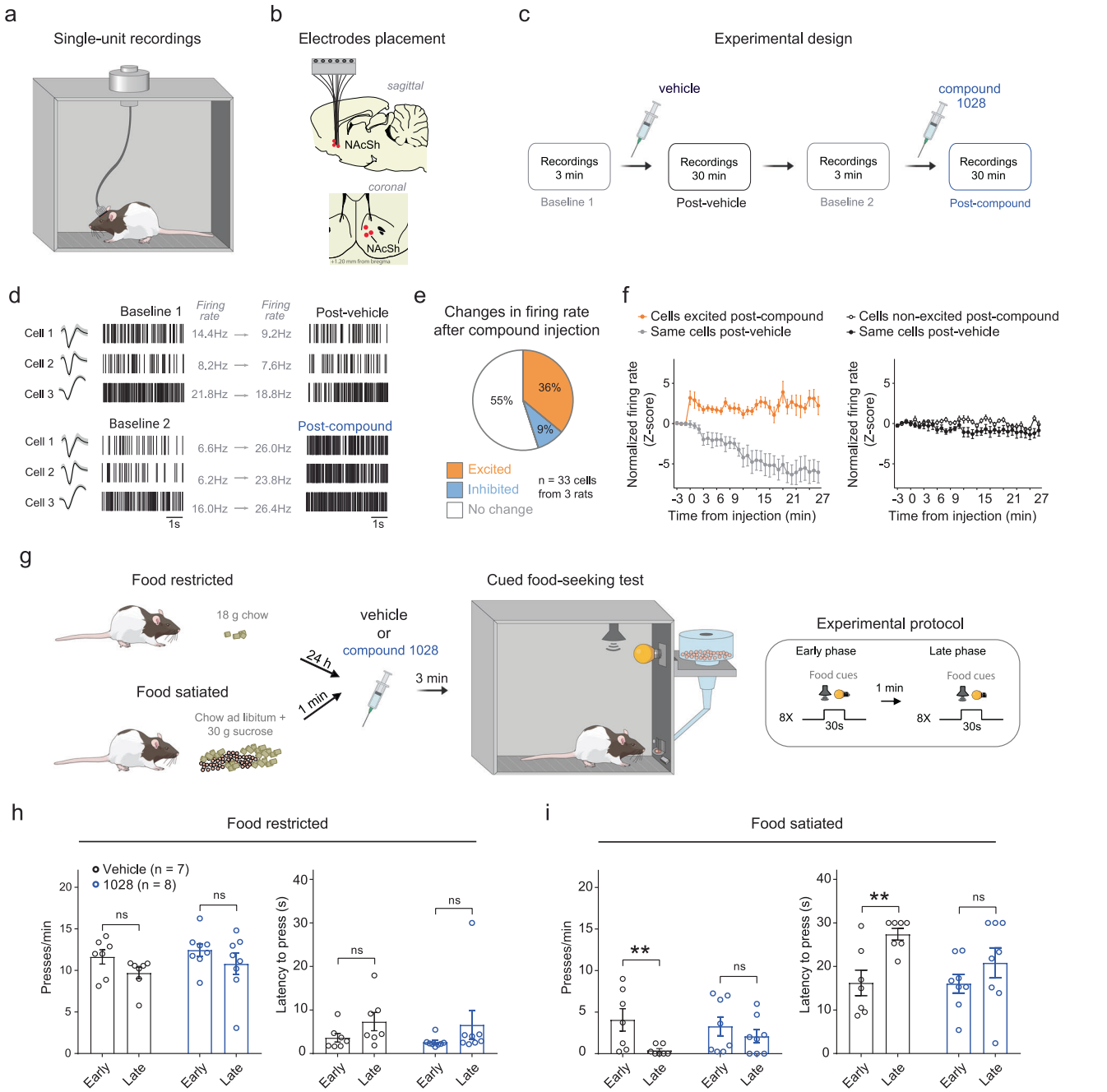

Fig. 8 | Systemic administration of 1028 changes the firing rates of NAc neurons and maintains food seeking motivation during a satiated state. a Behavioral chamber used during single-unit recordings. **b** Diagram showing the electrode placement. **c** Schematic drawing showing the timeline for the injections and recording sessions. **d** Raster plots and waveforms of three representative accumbal neurons across the recording sessions. **e** Pie chart summarizing changes in accumbal firing rates after the administration of 1028. Excited neurons: Z-score > 2.58, inhibited neurons: Z-score < −1.96. **f** Average normalized firing rate of accumbal neurons excited (left, 12 out of 33 neurons) or non-excited (right, 21 out of 33 neurons) following 1028 administration (5 mg/kg, IP) compared to the same neurons following vehicle administration ($n = 33$ neurons). **g** Schematic drawing of the cued food-seeking test used for food-restricted and food-satiated rats exposed to the same experimental protocol after the injection of vehicle or 1028. **h** Number of lever presses per minute during the food cue (left) and latency to press the lever after the food cue onset (right) during early vs. late phases of the session after the systemic injection of vehicle or 1028 (5 mg/kg, IP) in food-restricted rats. **i** Same as in (**h**) but for food-satiated rats. Data are shown as mean ± SEM. Two-way ANOVA followed by Sidak's multiple comparisons: ns, not significant; ** $p < 0.01$. In (**i**) left, $p = 0.0089$ (vehicle) and $p = 0.4351$ (1028). In (**i**) right $p = 0.0051$ (vehicle) and $p = 0.2134$ (1028). Source data are provided as a Source Data file. Illustrations were initially done using Mind the Graph and further modified using Adobe Illustrator.

less for food late in the session compared to early in the session ($p = 0.0172$ for the vehicle; $p = 0.0222$ for 1028; Supplementary Fig. S12), indicating the development of decreased lever press motivation within the session for the two groups. During the food-restricted condition test, there was also a significant main effect of time ($F(1,13) = 10.51$; $p = 0.0064$); although neither groups treated with vehicle nor treated with 1028 displayed a significant reduction in lever pressing rate within the session (Sidak's multiple comparisons, vehicle: $p = 0.0632$; 1028: $p = 0.0941$; Fig. 8h, left), indicating that lever press motivation was unchanged within the session for the two groups. This finding in the food-restricted test condition is further supported by a lack of main effect of time as it relates to latency to press (F

https://doi.org/10.1038/s41467-024-55554-7

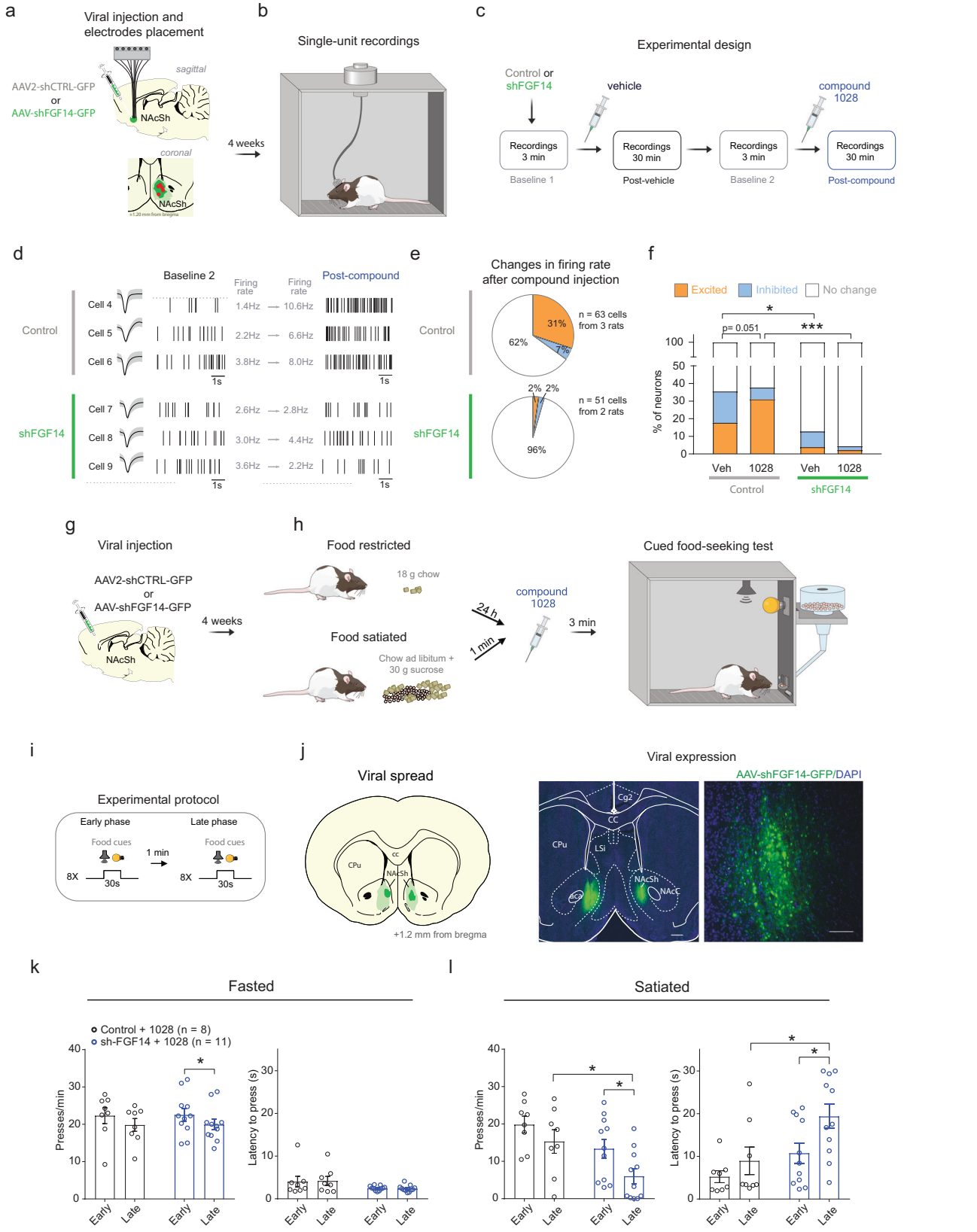

(1,13) = 3.095; $p = 0.1020$; Fig. 8h, right). In the satiated condition test, there was a main effect of time (F (1,13) = 11.11; $p = 0.0054$), but only rats treated with vehicle displayed a significant reduction in lever pressing rate late in the session compared to early in the session (Sidak's multiple comparisons, vehicle: $p = 0.0089$; 1028: $p = 0.4351$; Fig. 8i, left), suggesting that 1028 is able to prevent the decrease in motivation observed within the session for rats treated with vehicle. This finding in the food-satiated condition is further supported by the main effect of time in relation to latency to press (F (1,13) = 15.04; $p = 0.0019$), with only rats treated with vehicle displaying an increased latency to press late in the session versus early in the session (Sidak's multiple comparisons, vehicle: $p = 0.0051$; 1028: $p = 0.2134$; Fig. 8i,

Fig. 9 | Knockdown of FGF14 in the NAc blocks the effect of 1028 on food-seeking motivation. a–c Diagrammatic representation of experimental design and spread of viral expression (**a**), the chamber used during single-unit recordings (**b**), and schematic showing the timeline for the injections and recording sessions (**c**). **d** Raster plots and waveforms of three accumbal neurons recorded from rats injected with the control virus or the shFGF14 virus in the NAcSh. **e** Pie charts summarizing changes in accumbal firing rates after the administration of 1028 in the control or shFGF14 groups. Excited neurons: Z-score > 2.58, inhibited neurons: Z-score < − 1.96. **f** Stack bar showing the percentage of neurons that were excited, inhibited, or did not change their firing rates after the administration of vehicle or 1028 in both control or shFGF14 groups (two-tailed Chi-square test, *** $p < 0.0001$). **g–i** Diagram showing the viral vectors and local of injections (**g**), schematic of the cued food-seeking test (**h**), and protocol for the cued food-seeking test (**i**). **j** Diagram showing the minimum (dark green) and maximum (light green) spread of viral expression in the NAc and representative micrographs showing the viral expression in NAc. **k** Number of lever presses per minute during the food cue (left) and latency to press the lever after the food cue onset (right) during early vs. late phases of the session after the systemic injection of 1028 (5 mg/kg, IP) in food-restricted rats previously infused with AAV-shCTRL-GFP or AAV-shFGF14-GFP in the NAc ($n = 8$ rats for AAV-shCTRL-GFP + 1028; $n = 11$ rats for AAV-shFGF14-GFP +1028). **l** Same as in (**k**), but for food-satiated rats ($n = 8$ rats for AAV-shCTRL-GFP + 1028; $n = 11$ rats for AAV-shFGF14-GFP + 1028). Data are mean ± SEM. Two-way ANOVA followed by Sidak's multiple comparisons: * $p < 0.05$. In 9k, left, $p = 0.1101$ (shCTRL + 1028) and $p = 0.0439$ (shFGF14 + 1028). In 9l, left, $p = 0.1501$ (shCTRL + 1028) and $p = 0.0265$ (shFGF14 + 1028). In 9l, right, $p = 0.2731$ (shCTRL + 1028) and $p = 0.0167$ (shFGF14 + 1028). Source data are provided as a Source Data file. Illustrations were initially done using Mind the Graph and further modified using Adobe Illustrator.

right). Ensuring that changes in locomotive behavior were not a confound to our operant behavioral testing of 1028, we found that 1028 treatment affected neither the total distance traveled (Supplementary Fig. S13a) nor the average speed (Supplementary Fig. S13b).

To verify if the increased accumbal firing rate induced by 1028 treatment was dependent on the ligand's binding to FGF14 protein in the NAc, we infused bilaterally into the NAc the viral vector AAV2-shFGF14-GFP to knockdown FGF14, or the control viral vector AAV2-shCTRL-GFP, and implanted a single-unit recording electrode into the same region to measure the spontaneous firing rates of NAc neurons after IP injection of vehicle followed by compound 1028 (5 mg/kg, IP; Fig. 9a–c). To verify that AAV2-shFGF14-GFP efficiently knocked down FGF14 in the NAc, we stereotaxically injected either AAV2-shCTRL-GFP or AAV2-shFGF14-GFP into the NAc. Three weeks following surgery, NAc tissue samples were collected, and qRT-PCR was performed. As shown in Supplementary Fig. S14, the AAV2-shFGF14-GFP vector resulted in a marked reduction of FGF14 mRNA in the NAc, consistent with the knockdown efficiency of our previously published and validated viral vectors[50]. After waiting a period of four weeks for viral expression, we found that 31% (20 out of 63 neurons) of the recorded NAc cells displayed a significant increase (Z-score > 2.58) in firing rates following 1028 administration in the AAV2-shCTRL-GFP group, whereas only 2% of the recorded NAc cells increased their activity following compound 1028 injection in the AAV2-shFGF14-GFP group (2 out of 51 neurons, Fisher Exact test, $p < 0.0001$, Fig. 9d, e). Notably, following vehicle injection, NAc neurons from AAV2-shFGF14-GFP animals showed reduced firing rates compared to those from AAV2-shCTRL (Chi-square, $p = 0.0246$, Fig. 9f), indicating a role of endogenous FGF14 activity in regulating firing rates of NAc neurons in vivo.

To further investigate if the increased reward-seeking motivation induced by 1028 treatment depends on the presence of FGF14 protein in the NAc, we infused the same viral vectors AAV2-shFGF14-GFP or AAV2-shCTRL-GFP bilaterally into the NAc before exposing the animals to the same cued sucrose-seeking protocol described above (Fig. 9g–i). After waiting a period of four weeks for viral expression, we observed sufficient fluorescent labeling in NAc cells (Fig. 9j). During baseline for the restricted condition, AAV2-shCTRL-GFP and AAV2-shFGF14-GFP treated rats displayed similar lever pressing measures (Supplementary Fig. S15), indicating that knockdown FGF14 had no effect in reward-seeking motivation per se. A trial-by-trial analyses across the session revealed a small but significant reduction in lever presses when comparing the first two to the last two food cue presentations ($F(5.881, 129.4) = 2.251$, $p = 0.0435$; Sidak's multiple comparison test, cue 2 = 23.3 presses/min vs. cue 15 = 17.9 presses/min, adjusted $p = 0.015$; cue 2 = 23.3 presses/min vs. cue 16 = 17.3 presses/min, adjusted $p = 0.0037$), indicating the development of decreased lever press motivation within the session in both groups. During the food-restricted test condition the following day, there was a significant main effect of time across the session for lever presses per minute (Time factor, $F(1, 17) = 10.17$; $p = 0.0054$), but not latency to press (Time factor, $F(1,17) = 0.02871$; $p = 0.8674$). A Sidak's multiple comparison test showed no differences in lever presses per minute across the session for AAV-shCTRL-GFP rats treated with 1028 ($p = 0.1101$; Fig. 9k), indicating that lever-press motivation was maintained throughout the session. While this result seems to disagree with those described above in Fig. 8h, which showed no effect of compound 1028 under food restriction, one possible explanation is the observation that the AAV-shCTRL-GFP group in this experiment displayed a partial reduction in food-seeking motivation within the session (Supplementary Fig. S15). Conversely, AAV-shFGF14-GFP rats treated with 1028 displayed a significant decrease in lever presses within the session ($p = 0.0439$; Fig. 9k), indicating that the efficacy of compound 1028 to maintain reward-seeking motivation throughout the session was impaired by silencing FGF14 in the NAc. In the satiated test condition, there was a significant main effect of time and group for presses per minute (Time factor, $F(1,17) = 18.89$; $p = 0.0004$; Group factor: $F(1, 17) = 5.747$; $p = 0.0283$) and latency to press ($F(1,17) = 9.745$; $p = 0.0062$; Group factor: $F(1, 17) = 6.394$; $p = 0.0216$). A Sidak's multiple comparison test did not reveal differences in lever presses per minute ($p = 0.1501$; Fig. 9l, left) or latency to press ($p = 0.2731$; Fig. 9l, right) across the session for AAV-shCTRL-GFP rats treated with 1028, indicating maintenance of lever press motivation within the session. Notably, AAV-shFGF14-GFP rats treated with 1028 displayed significantly decreased lever press frequency ($p = 0.0265$; Fig. 9lf, left) and increased latency to press ($p = 0.0167$; Fig. 9l, right) late in the session versus early in the session, indicating that the efficacy of 1028 to maintain reward-seeking motivation across the session was blocked by knockdown of FGF14 in the NAc. Together, these experiments demonstrate that intact expression of FGF14 in the NAc is essential for mediating the effects of 1028 on reward-seeking motivation. This applies to both satiated animals experiencing a prolonged lack of motivation and fasted animals encountering a rapidly developing reduction in motivation within the session.

1028 modulates accumbal dopamine levels

MSN activity regulates DA signaling in the NAc through direct and indirect connections with interneurons and dopaminergic cells of the VTA[14,18], and through modulation of local circuit components within the NAc, such as those involving CIN regulation of local dopamine release[15–17]. Given the increase in NAc neuron activity caused by 1028, we next investigated if this change would alter dopaminergic signaling in the NAc. To do so, we assessed the effects of 1028 on striatal extracellular dopamine (DA) levels during operant conditioning in mice. We opted to assay 1028 in mice for fiber photometry studies to ensure the inter-species in vivo efficacy of the compound. For in vivo DA release measurement, we expressed the genetically encoded fluorescent DA indicator GRAB-DA2m[51,52] and the control red fluorophore mRuby2 separately in the medial shell portion of the NAc (medNAcSh) and dorsal lateral striatum (DLS) in both hemispheres of wild-type mice (Fig. 10a). Animals underwent initial lever press training

https://doi.org/10.1038/s41467-024-55554-7

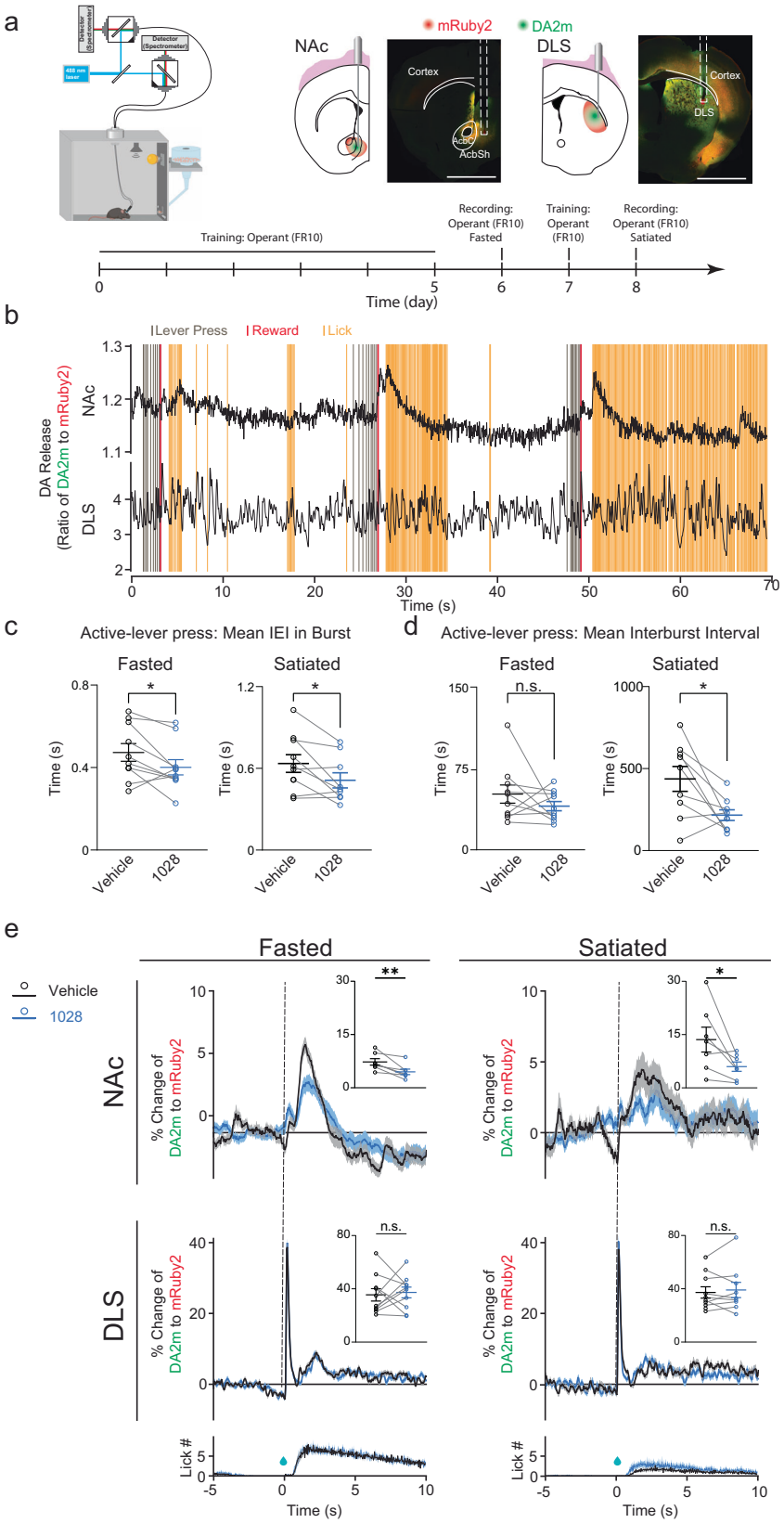

on a fixed-ratio 10 (FR10) schedule before the beginning of the fiber photometry recording session during operant conditioning.

Using spectrally resolved fiber photometry[53], we simultaneously recorded from the NAc and DLS throughout operant conditioning (Fig. 10b). We observed that the fluorescence ratio of DA2m to mRuby2 increased when the reward was delivered in both the NAc and DLS. However, the increased DA response to reward consumption was only evident in the NAc (Fig. 10b). Injection of either the vehicle or 1028 (5 mg/kg, IP) was administered 10 minutes before the operant sessions with fiber photometry recording to study the effects of 1028 on striatal DA during operant conditioning. We used burst analysis of lever press to assess motivation, in which reduced inter-event interval (IEI) time

Fig. 10 | 1028 selectively reduces dopamine levels in the medial nucleus accumbens shell during reward consumption. a Schematic illustration of fiber photometry recording in an operant chamber (top-left) and immunofluorescence images (top-right) of green fluorescent DA sensor DA2m and red fluorescent protein mRuby2. The core and shell of the nucleus accumbens, cortex, and DLS were indicated with the solid line. Optical fiber tips were indicated with the dashed line. Experimental timeline (bottom). In this particular immunostaining experiment, DA2m is labeled with Alexa Fluor 488 secondary antibody, whereas mRuby2 is unstained and visualized by its endogenous fluorescence. Scale: 1000 μm. **b** The dynamic changes of extracellular DA levels in the NAc (top) and DLS (bottom), represented by the fluorescence ratio of DA2m to mRuby2 in a mouse performing operant conditioning. The time points of lever press, reward, and lick were indicated by blue, red, and orange, respectively. **c**, **d** Comparison of the effect of 1028 versus vehicle on inter events interval (IEI) (**c**) and inter-burst interval (**d**) of active-lever press in operant conditioning. Left, fasted mice; right, satiated mice. **e** Changes of fluorescence ratio of DA2m to mRuby2 in NAc (top-left, fasted mice; top-right, satiated mice) and DLS (mid-left, fasted mice; mid-right, satiated mice), aligned to reward delivery, together with lick (bottom-left, fasted mice; bottom-right, satiated mice). The sucrose drop indicates the time point of reward delivery. All data are plotted as mean ± SEM overlaid with individual replicates. n. s., $p > 0.05$; *, $p < 0.05$; **, $p < 0.01$, two-tailed paired t test. $n = 7$ mice for NAc, $n = 10$ mice for DLS and $n = 10$ mice for active-lever press and lick, except $n = 9$ for active-lever press in satiated mice. Source data are provided as a Source Data file. In (**c**) $p = 0.0455$ (fasted) and $p = 0.0221$ (satiated). In (**d**) $p = 0.2736$ (fasted) and $p = 0.0215$ (satiated). In (**e**) top, $p = 0.0095$ (fasted) and $p = 0.0418$ (satiated). In (**e**) bottom, $p = 0.7561$ (fasted) and $p = 0.8491$ (satiated). Illustrations were initially done using Mind the Graph and further modified using Adobe Illustrator.

within bursts and smaller inter-burst intervals were interpreted as increased reward-seeking motivation. We observed that administration of 1028 significantly reduced IEI time within bursts in both food-restricted and food-satiated mice when compared to vehicle-treated mice (food restricted: vehicle = 0.47 ± 0.04, 1028 = 0.40 ± 0.04; food satiated: vehicle = 0.64 ± 0.06, 1028 = 0.51 ± 0.06; Fig. 10c). Additionally, 1028 administration reduced the inter-burst interval time in satiated mice (vehicle = 436.84 ± 75.88; 1028 = 216.18 ± 32.54) with no changes during food-restricted conditions (vehicle = 51.48 ± 8.37; 1028 = 40.35 ± 4.27; Fig. 10d), consistent with the preferential effects of 1028 in food satiated conditions observed above. We further analyzed the fluorescence ratio of DA2m to mRuby2 from both the NAc and DLS, using the timepoint of reward delivery as a reference. In the NAc, a larger DA signal was induced by the onset of a sequence of licks after reward delivery (reward consumption) compared to the reward delivery itself, and the DA signal in the NAc during reward consumption was significantly decreased by 1028 in both food restricted and food satiated mice (food restricted: vehicle = 7.32 ± 0.91, 1028 = 4.51 ± 0.77; food satiated: vehicle = 13.59 ± 3.51, 1028 = 5.98 ± 1.32; Fig. 10e). On the other hand, in the DLS, the DA signal was larger in response to reward delivery, and this DA signal was not affected by 1028 (for fasted, vehicle = 35.47 ± 4.62, 1028 = 37.27 ± 4.02; satiated, vehicle = 37.23 ± 4.26, 1028 = 39.08 ± 5.72; Fig. 10e). Collectively, these results further highlight that 1028 increases reward-seeking motivation preferentially during unmotivated states and shows that 1028 is able to modulate dopaminergic signaling in the NAc while not affecting DA signaling in the DLS.

Discussion

We have previously established that the FGF14/$Na_v1.6$ PPI interface has druggable regions[43] that can be pharmacologically targeted by using peptides and peptidomimetics (reviewed in Dvorak et al. 2021[54]). While useful for probing the FGF14/$Na_v1.6$ complex in vitro, these peptides and peptidomimetics display low potency and poor drug-like properties. Thus, in the present study, we sought to build upon our previous findings and develop brain penetrant, small molecules targeting the FGF14/$Na_v1.6$ complex that displayed improved potency and drug-like properties. Through a high-throughput screening of ~45,000 commercially available compounds from the Maybridge and Chembridge libraries, we identified an initial lead compound (7605), which displayed single-digit micromolar potency and favorable properties for CNS drug discovery[34]. Lead optimization of 7605 produced 1028, which displayed high nanomolar potency and blood-brain barrier penetrance. Our discovery of a brain penetrant modulator of a PPI in the CNS demonstrates that PPIs can be amenable to small molecule modulation in the brain, which points toward hundreds of untapped drug targets that could be pharmacologically targeted in an effort to expand the druggable genome.

Functionally, we found that 1028 gives rise to targeted effects on the voltage dependence of steady-state inactivation of $Na_v1.6$-mediated I_{Na}. Specifically, we found that 1028 causes a dose-dependent, depolarizing shift in the voltage-dependence of inactivation of I_{Na} in HEK293 cells expressing $Na_v1.6$ and FGF14 with potency in the high nanomolar range. In contrast, 1028 did not exert effects on the I_{Na} of HEK293 cells expressing $Na_v1.1$ and FGF14 or $Na_v1.2$ and FGF14 when tested at 1 μM. Previous reports have indicated that the interaction between the EF-hand domain of the CTD and the III-IV linker is important for controlling the voltage dependence of steady-state inactivation of I_{Na}[45,46]. We, therefore, hypothesized that this interaction could be important in terms of conferring 1028's regulatory effects on Nav1.6 channel inactivation. Consistent with our hypothesis, destabilization of the interaction between the III-IV linker and CTD blocked the effects of 1028 on $Na_v1.6$ channel inactivation. Notably, for all Na_v channel isoforms, except $Na_v1.6$ and $Na_v1.9$, the putative interaction between the III-IV linker and CTD involves a lysine and glutamate, respectively, whereas, for $Na_v1.6$ and $Na_v1.9$, the putative interaction involves a lysine and aspartate[46]. Despite representing a subtle difference, lysine-glutamate interactions are more rigid in terms of their conformation compared to lysine-aspartate interactions[55]. Thus, one possibility is that the increased flexibility of the interaction between the III-IV linker and CTD of the $Na_v1.6$ channel conferred by the lysine-aspartate interaction causes the channel to be more susceptible to 1028's regulatory effects. This difference in the amino acids involved in the intramolecular interaction between the III-IV linker and CTD for the $Na_v1.6$, coupled with our modeling suggesting that 1028 is accessible to $FGF14^{R117}$ when FGF14 is in complex with $Na_v1.6$, but not when FGF14 is in complex with $Na_v1.1$ or $Na_v1.2$, could serve as the basis for the compound's selective regulation of the $Na_v1.6$ channel in the presence of FGF14.

Consistent with 1028's effects on $Na_v1.6$ channel inactivation in heterologous cells, 1028 also induced a dose-dependent depolarizing shift in the voltage-dependence of inactivation of the I_{Na} of MSNs with high nanomolar potency. As this effect on inactivation would be expected to hamper $Na_v1.6$ channel closure, and, thereby, give rise to a prolonged inward flux of Na^+ into the cell, we hypothesized that 1028 would increase the intrinsic excitability of MSNs. Consistent with this hypothesis, 1028 caused a dose-dependent increase in the maximal firing and IFF of MSNs with high nanomolar potency, consistent with the compound's dose-responsive regulation of $Na_v1.6$ channel inactivation. Providing mechanistic insight into 1028's excitatory effects on the intrinsic excitability of MSNs, we found that 1028 increased MSN firing through a $FGF14^{R117}$-dependent mechanism, consistent with 1028's protein-ligand binding relationship with FGF14 being dependent upon R117. Notably, the R117 residue of FGF14 has previously been shown to be important for conferring FGF14's regulatory effects on the I_{Na} and excitability of cerebellar Purkinje neurons[56]. In addition, in our AF2 model of the FGF14/$Na_v1.6$ PPI interface, $FGF14^{R117}$ has a predicted interaction with $Na_v1.6^{D1846}$, which is predicted to form a salt bridge with $Na_v1.6^{R1866}$. This is consistent with the previously published crystal structure of the FGF13/$Na_v1.5$ CTD complex, which shows an

interaction between the corresponding residues of FGF13 (R57) and $Na_v1.5$ (D1852)[57]. Crystallographic studies have also shown that when FGF13 is in complex with the CTD of the $Na_v1.5$ channel, there is uncoupling of the EF-hand domain and IQ domain[44], the former of which is involved in the intramolecular interaction with the III-IV linker and, thereby, affects the voltage-dependence of steady-state inactivation[45]. Considering these structural studies in the context of our molecular modeling, LCA, SPR, and electrophysiological studies of 1028, one plausible explanation of 1028's mechanism of action is that the compound, when bound to FGF14 and in complex with the $Na_v1.6$ CTD, contributes to further destabilization of the EF-hand and IQ domains caused by FGF14, enabling the EF-hand domain to more readily interact with the III-IV linker, thereby leading to a depolarizing shift in the voltage-dependence of inactivation that would hamper $Na_v1.6$ channel closure and increase the excitability of MSNs. While our electrophysiological data provide evidence for this pharmacodynamic hypothesis, future structural studies are necessary to unequivocally confirm this putative mechanism of 1028 in controlling Na_v channel inactivation.

We were able to recapitulate the results of our ex vivo electrophysiological testing of 1028 in vivo, as single-unit recordings revealed increased firing rates of accumbal neurons after 5 mg/kg IP injection of 1028 in rats. Behaviorally, these electrophysiological changes correlated with increased motivation to seek reward preferentially during unmotivated situations. Our in vivo electrophysiological and behavioral results are consistent with previous studies showing that activation of D1 and D2 MSNs enhance motivational drive toward natural rewards during the presentation of reward-associated cues[48,49,58]. Our subsequent observation that silencing FGF14 in the NAc blocks the increased firing rate, and the augmented behavioral motivation induced by 1028 administration demonstrates that the ligand's interaction with FGF14 is required for the in vivo effects, providing compelling evidence for 1028 target engagement.

Notably, compound 1028 increases motivation preferentially during motivation-deficient conditions, as we observed larger increases in reward-seeking responses in food-satiated conditions. Although the exact mechanism behind 1028's differential impact on motivation under varied feeding conditions remains unclear, it's possible that intracellular signaling pathways responsive to metabolic states influence interactions between the $Na_v1.6$ channel and its auxiliary proteins. For instance, glycogen synthase kinase 3 beta (GSK3β), a key player in metabolism[59], regulates FGF14/$Na_v1.6$ complex assembly. Inhibition of GSK3β, which occurs under food-restricted conditions[59], reduces FGF14/$Na_v1.6$ complex assembly[60]. In food-restricted rats, this inhibition of GSK3β may decrease FGF14/$Na_v1.6$ complex assembly, impairing 1028's ability to regulate neuronal function and masking its behavioral effects. Further studies are needed to investigate how changes in intracellular signaling pathways during different metabolic states may contribute to 1028's preferential activity during satiated conditions.

Providing a potential mechanism that links 1028's effect on accumbal neuron firing to its effect on motivation-related behaviors, we found that 1028 decreases NAc DA levels. Although the mechanism driving this change in DA levels is presently unknown, one possibility is that 1028's effects on MSN firing cause changes in the mesolimbic dopamine pathway. In the medial nucleus accumbens shell (medNAcSh), the subnuclei where the fiber photometry recordings were performed, D1 MSNs primarily project onto dopaminergic neurons of the VTA[18], whereas D2 MSNs of the medNAcSh mainly target GABAergic neurons in the ventral pallidum (VP), which synapse onto VTA dopaminergic neurons[61–63]. Considering the results of our fiber photometry studies, one possibility is that when tested in vivo, 1028 has a preferential effect on D1 MSNs in the medNAcSh and their direct projections to the VTA, outweighing the effects on D2 MSNs and their indirect connections with the VTA, and leading to a reduction in DA release during reward consumption. To test this potential mechanism, future studies could employ circuit tracing of D1/D2 connections with the VTA and investigate the neural activity of the specific projections following the 1028 administration. In addition, behavioral testing of 1028 in conditions in which D1 MSNs or D2 MSNs are optogenetically silenced could aid in understanding the precise circuitry mechanism by which 1028 produces effects on reward-seeking behavior. Another possibility by which 1028 might reduce NAc DA levels is through modulation of local circuit components within the NAc. Chief among such local circuit components that could be modulated by 1028's effects on MSN function that could control DA levels are CINs. There neurons have previously been shown to release ACh onto dopaminergic axons that innervate the NAc[64]. Notably, dopaminergic axons that innervate the NAc express nicotinic ACh receptors (nAChR), and activation of these receptors can locally evoke action potentials in DA axons, facilitating local dopamine release in the NAc[15]. Moreover, recent studies have also found that directly activating CINs of the NAc increases NAc dopamine levels[16]. Pertinent to the present investigation, activation of striatal MSNs has been shown to inhibit the excitability of CINs[17,65–67], Thus, one possibility for how 1028 decreases DA levels in the NAc is through 1028's increase of accumbal neuron firing, ~ 95% of which are MSNs in the NAc, causing inhibition of CINs. This, in turn, would inhibit ACh release and reduce the activation of nAChRs on DA axons that innervate the NAc, thereby reducing local DA release in the NAc. Given that this possible mechanism by which 1028 regulates DA levels is indirect and mediated through MSN regulation of CIN excitability, this could explain why the effect of 1028 on DA levels is comparatively small relative to the compound's effects on MSN excitability.

In considering 1028's therapeutic potential and side effects, prior studies show that in mice vulnerable to chronic social defeat stress (CSDS) and depression-like behaviors, D1 MSNs are hyperexcitable compared to resilient mice[68]. Interestingly, despite this link between D1 MSN hyperexcitability and CSDS susceptibility, optogenetic activation of D1 MSNs in susceptible mice was found to alleviate depression-like behaviors[68]. Thus, D1 MSN hyperexcitability may contribute to CSDS vulnerability, while D1 MSN activation may also counteract depression-like symptoms. Thus, any preferential activity of 1028 on D1 MSNs should be carefully evaluated to identify an optimal therapeutic window for 1028 derivatives, aiming to minimize side effects.

Overall, using a combination of high-throughput screening and medicinal chemistry, we developed a brain penetrant modulator of the FGF14/$Na_v1.6$ that displays nanomolar potency. Using patch-clamp electrophysiology, we showed that the compound selectivity regulated the FGF14/$Na_v1.6$ complex and caused targeted effects on the voltage-dependence of inactivation of $Na_v1.6$-mediated I_{Na}, leading to potentiation of the intrinsic excitability of MSNs of the NAc. In vivo, we reproduced the effects of the compound on accumbal firing and showed that the electrophysiological changes were concomitant with increases in reward-seeking motivation, as well as modifications in DA signaling in the NAc, preferentially during unmotivated conditions. Collectively, these results demonstrate that the FGF14/$Na_v1.6$ complex is a tractable pharmacological target for psychiatric disorders that are characterized by deficits in motivation and altered dopamine signaling.

Methods

Animals were housed, $n \leq 5$ per cage, with a 12 h light/12 h dark cycle with food and water ad libitum, except where otherwise noted. Animals were humanely euthanized via an overdose of isoflurane followed by decapitation. For patch-clamp studies involving mouse brain slices, all surgical and experimental procedures were approved by the University of Texas Medical Branch Institutional Animal Care and Use Committee (protocol number: 0904029D, Laezza). For in vivo single

unit recordings and rat behavioral studies, all surgical and experimental procedures were approved by the Center for Laboratory Animal Medicine and Care of the University of Health Science Center at Houston (protocol number: AWC-22-0094, Do Monte). For fiber photometry and mouse behavioral studies, all surgical and experimental procedures were approved by the US National Institute of Environmental Health Sciences Animal Care and Use Committee (protocol number: ASP#2015-0013, Cui).

DNA Constructs

The FGF14-NLuc, CLuc-FGF13, CLuc-FGF14^{WT}, CLuc-FGF14^{R117A}, CD4-Na$_v$1.6 CTD^{WT}-NLuc, CD4-Na$_v$1.6 CTD^{D1846A}-NLuc, CD4-Na$_v$1.6 CTD^{R1866A}-NLuc, CD4-Na$_v$1.6 CTD$^{D1846A+R1866A}$-NLuc, CD4-Na$_v$1.2 CTD-NLuc, pET28a-FGF14, pET28a-FGF14^{R117A}, pET30a-Nav1.6 CTD, and pQBI-FGF14-GFP constructs were engineered and characterized as previously described[23,30]. The plasmid pGL3 expressing full-length firefly (*Photinus pyralis*) luciferase was a gift from Dr. P. Sarkar (Department of Neurology, UTMB). The Na$_v$1.6 α subunit cDNA, β_1 subunit cDNA, and β_2 subunit cDNA were gifts from Dr. Geoffery S. Pitt (Cardiovascular Research Unit, Weill Cornell Medicine). Na$_v$1.6 channel mutants were designed and developed by GeneArt.

Cell culture

HEK293 cells were purchased from ATCC (Manassas, CA, USA, catalog number CRL-1573). HEK293 cells were maintained as previously described[30]. For transfection of cells to be used for LCA studies, cells were seeded in 24-well CELLSTAR® tissue culture plates (Greiner Bio-One, Monroe, NC, USA) at 4.5×10^5 cells per well and incubated overnight to give monolayers at 90–100% confluency. The cells were then transiently transfected with the pair of CLuc-FGF14 and CD4-Nav1.6-C-tail-NLuc constructs or the full-length *Photinus pyralis* luciferase construct (pGL3) using Lipofectamine 2000 (Invitrogen, Waltham, MA, USA), according to the manufacturer's instructions. 1 μg of each plasmid was used per transfection per well. We have previously described our development of a double stable HEK293 cell line expressing recombinant CD4-Nav1.6-NLuc and CLuc-FGF14 protein[23], and these cells were maintained under 0.5 mg/mL geneticin G418 and 5 μg/mL puromycin.

The HEK293-Na$_v$1.1-FGF14-GFP, HEK293-Na$_v$1.2-FGF14-GFP, and HEK293-Na$_v$1.6-FGF14-GFP double stable cell lines were developed by VectorBuilder and were validated at the source for transgene expression using qPCR. These cells were maintained similarly to HEK293 cells, with the caveat that the growth media was supplemented with 500 μg/mL of G418 and 5 μg/mL puromycin to ensure stable Na$_v$ and FGF14 protein expression, respectively. For electrophysiological experiments requiring transient transfection of the Na$_v$1.6 channel α subunit, HEK293 cells were transiently transfected with Na$_v$1.6^{WT} or mutant cDNA, along with β_1 subunit, β_2 subunit, and FGF14-GFP cDNA at a 10:3:3:3 ratio. Recordings were performed 24–36 h after transfection in only GFP-positive cells.

ND7-23 cells were purchased from Sigma-Aldrich (St. Louis, MO, USA, catalog number 92090903). Cells were cultured similarly to HEK293 cells, with the caveat that the medium was comprised of DMEM (Invitrogen), 2 mM glutamine, and 10% FBS (Invitrogen).

Split-luciferase complementation assay

96-well plate assay. Cells were trypsinized (0.25%), triturated in a medium, and seeded in white, clear-bottom CELLSTAR μClear® 96-well tissue culture plates (Greiner Bio-One) at ~10^5 cells per well in 200 μL of medium.

For transiently transfected cells, the trypsinization occurred 48 hours post-transfection. The cells were incubated for 24 h, and the growth medium was subsequently replaced with 100 μL of serum-free, phenol red-free DMEM/F12 medium (Invitrogen) containing compounds or vehicle (DMSO). The final concentration of DMSO was maintained at 0.5% for all wells. Following 2 h incubation at 37 C, the reporter reaction was initiated by injection of 100 μL substrate solution containing 1.5 mg/mL of D-luciferin dissolved in PBS (final concentration = 0.75 mg/mL) by the Synergy™ H4 Multi-Mode Microplate Reader (BioTek, Winooski, VT, USA). Luminescence readings were performed at 2-minute intervals for 20–30 min, the integration time of 0.5 s, and the cells were maintained at 37 °C throughout the measurements. Signal intensity for each well was calculated as a mean value of peak luminescence; the calculated values were expressed as a percentage of mean signal intensity in the control samples from the same experimental plate.

384-well plate assay. Cells were trypsinized (0.25%), triturated in a medium, and seeded in white, clear-bottom CELLSTAR μClear® 384-well tissue culture plates (Greiner Bio-One) at 30,000 (3×10^4) cells per well in 40 μL of serum-free, phenol red-free DMEM/F12 medium using the Multidrop Combi (Thermo Fisher, Waltham, MA, USA). The LabCyte Echo 550 was used to acoustically deliver nanoliter volumes of compounds and DMSO. The final concentration of DMSO was maintained at 0.3% for all wells. Following 2 h incubation at 37 C, the reporter reaction was initiated by injection of 40 μL substrate solution containing 1.5 mg/mL of D-luciferin (final concentration = 0.75 mg/mL) by the Multidrop Combi. After 1 h incubation, the Tecan Infinite M1000 was used to detect luminescence. Detailed methods for LCA can be found in previous studies[23,30].

Dose-response curves were obtained using GraphPad Prism 8 by fitting the data with a non-linear regression:

$$A + \frac{B - A}{1 + 10^{\log(x_0 - x)H}}$$

where x is log10 of the compound concentration in M, x_0 is the inflection point (EC_{50} or IC_{50}), A is the bottom plateau effect, B is the top plateau effect, and H is the Hill slope.

Screened libraries

ChemBridge DIVERSet-1 (30,080 compounds). A subset of the predesigned collection of up to 52,000 drug-like small molecules. The set was rationally selected by ChemBridge based on 3D pharmacophore analysis to cover the broadest part of biologically relevant pharmacophore diversity space. A highly recognized and proven primary screening tool for a wide range of both validated and new biological targets. Compounds are present at 10 mM in DMSO (3.3 mg/mL median amount).

Maybridge HitFinder Collection (14,400 compounds). The HitFinder Collection maintains the structural diversity of the Maybridge Screening Collection by using an industry-standard clustering algorithm based on Daylight Fingerprints and Tanimoto similarity to select a statistically representative sample of the full Collection of over 56,000 small molecules. Users of the HitFinder™ Collection, therefore, gain cost-effective access to the richness of the Maybridge Screening Compounds with rapid access to "hit" analogs for validation and follow-up studies. Compounds are present at 10 mM in DMSO.

Cell viability assay

The CellTiter-Blue (CTB) Cell Viability Assay (Promega) was used as a control to detect compounds causing cellular toxicity. Immediately following the luminescence reading, 10 μL of 1X CTB reagent was dispensed into 384-well plates, incubated overnight (16 h) at 37 C, and fluorescence was detected using the Tecan Infinite M1000 reader (excitation $\lambda = 560$ nm, emission $\lambda = 590$ nm). Cell viability was expressed as the percent mean fluorescent signal intensity in the control samples from the same experimental plate.

Hit scoring method

We observed batch effects associated with alterations in the variance in the negative control. For this reason, hit retrieval using a single Z-score cut-off is difficult. In order to account for this issue and minimize the false detection rate, we prioritized hits using a B-score method with cross-plate smoothing. In general, a B-score is similar to a Z-score; however, it takes well position and assay chronology into account in addition to activity[25,69]. A critical assumption associated with B-scores is that the majority of wells are inactive on an assay plate, which is generally true for chemical diversity libraries. Inactive wells are then used to fit a local surface using an extension of Tukey's median-polish method. Furthermore, this method can also be applied to correct assay systematic alterations in the noise across assay plates in a larger screening campaign. This effectively factors in information from well positions across longitudinal plates into the median polishing algorithm. B-score normalization was performed using the Plate Analytics package in Pipeline Pilot (2018 Edition, Biovia). The parameters used to generate B-scores in this data set used a total of 10 iterations of median polishing across a 20-plate running window with a stringent (0.001) convergence threshold. Results are plotted in plate order, and B-score activity is color-coded.

Protein thermal shift assay

The FGF14^{WT}, FGF14^{R117A}, and $Na_v1.6$ CTD proteins used in this study for the protein thermal shift assay and surface plasmon resonance were expressed and purified as previously described[30,31]. The protein thermal shift assay was performed as previously described[31]. Briefly, reactions were prepared in 96-well PCR plates using the PTS Dye Kit (Applied Biosystems, Life Technologies, Waltham, MA, USA) as per manufacturer instructions, and the assay was conducted on a QuantStudio 3 rtPCR System. Each well included a total reaction volume of 20 µL comprised of 2 µg of FGF14 or $Na_v1.6$ CTD protein, 1X dye, and compounds (50 µM; $n = 4$ wells per condition) or 0.5% DMSO alone (control; $n = 8$ wells per plate) in PBS. Additional per-plate controls ($n = 4$ wells per condition) included buffer and dye alone (no protein control) and compounds alone (in the absence of protein) to assess potential interactions between compounds and fluorescent dye. The plate was heated from 25 to 99 °C at a ramp rate of 0.05 °C/s with ROX as the selected reporter. The Boltzmann method was used to obtain protein T_M.

Surface plasmon resonance spectroscopy

SPR experiments were performed on a Biacore T100 instrument (GE Healthcare, Pittsburgh, PA, USA). Proteins were immobilized on CM5 sensor chips using 10 mM sodium acetate buffer (pH 5.5) with the Amine Coupling Kit (GE Healthcare) as per the manufacturer's instructions, to a final RU value of 17,896 for FGF14 and 6800 for $Na_v1.6$ CTD. No protein was coupled to the control flow channels of the chip (Lanes 1 and 3). The interaction of experimental compounds against FGF14 and $Na_v1.6$ proteins was studied at 25 °C using a flow rate of 50 µl/min. Compounds were serially diluted (0.195–200 µM) in PBS supplemented with Tween-20 0.005% and 2% DMSO. Each sample was injected over the chip for 60–120 s, followed by a dissociation period of 120 s, and finally chip surface regeneration (600 mM NaCl, 5% DMSO) for 120 s. Compounds were tested with concentrations of 0.195, 0.39, 0.78, 1.56, 3.12, 6.25, 12.5, 25, 50, 100, and 200 µM, including 12.5 µM, 25 µM, and blanks (buffer alone) in duplicate. A DMSO calibration was performed for each experiment [1.5–2.8% (vol/vol) DMSO] to correct for bulk refractive index shifts[70]. For each compound injection, nonspecific responses (buffer alone) were subtracted from experimental sensorgrams/traces prior to data analysis. Kinetic data were analyzed using the Biacore T100 Analysis software. Following visual inspection of the binding curves, the equilibrium constant (K_D) was calculated using two methods: (1) maximal responses were plotted against compound concentration, and the steady state K_D was calculated from the fitted saturation binding curve; (2) a kinetic analysis of each ligand/analyte interaction was obtained by fitting the response data to the simplest Langmuir 1:1 interaction model ($K_D = k_{off}/k_{on}$). The kinetic constants generated from the fitted binding curves were assessed for accuracy based on the distribution of the residuals (even and near zero to baseline). Graphs were plotted in GraphPad Prism 8 Software (La Jolla, CA).

In silico blood-brain barrier permeability screening

To assess the BBB permeability of 7605, we employed a validated in silico atomic-detail molecular dynamics screening method, as previously described[71,72]. In brief, three-dimensional hit compound structures underwent energy minimization and parameterization under the CHARMM General Force Field (CGenFF)[73] before undergoing equilibrium molecular dynamics simulations using GROMACS[74] across a human BBB model membrane. Permeabilities were calculated from simulation trajectories, with compounds exceeding 10^{-5} cm/s (approximately the permeability of diazepam[75]) considered potential lead optimization candidates. These findings guided the selection of lead compounds for further experimental validation and optimization studies.

Synthesis of 1028

The detailed procedure for the synthesis of 1028 is shown in the Supplementary Information, along with its corresponding spectral data.

Structure prediction of FGF14/$Na_v1.1$, FGF14/$Na_v1.2$ and FGF14/$Na_v1.6$ complexes

Initially, the FASTA files containing the sequences of the first 150 amino acids of the CTD of $Na_v1.1$ (UniProtKB: P35498), $Na_v1.2$ (UniProtKB: Q99250), $Na_v1.6$ (UniProtKB: Q9UQD0), and FGF14 (amino acids 71-218) (UniProtKB: Q92915-2) were modeled using AlphaFold_2.0_multimer.v3 (AFM V3) via a Jupyter Notebook on Google Colab within ChimeraX[76,77]. Subsequently, the models were energy-minimized using the Chiron web server[78]. To validate the models, we performed superimposition onto the available X-ray crystal structures of iFGFs/Nav (PDB codes: 4JPZ, 4DCK, and 4JQ0) using PyMOL, ensuring an acceptable RMSD < 2 Å. The analysis of plDDT values for all three FGF14/$Na_v1.1$ (pLDDT = 88.3 pTM = 0.851 ipTM = 0.891), FGF14/$Na_v1.2$ (pLDDT = 89.8 pTM = 0.853 ipTM = 0.897), and FGF14/$Na_v1.6$ (pLDDT = 88.1 pTM = 0.846 ipTM = 0.892) complexes indicated a quality level of more than 88% confidence for the predicted protein structures. The similarity of $Na_v1.1$ and $Na_v1.2$ to $Na_v1.6$ is 77.62% and 77.17%, respectively.

Molecular docking of compound 1028

All AF protein structures (FGF14/$Na_v1.1$, FGF14/$Na_v1.2$, and FGF14/$Na_v1.6$) underwent preprocessing using the Schrödinger Suite 2023-4 protein preparation wizard (Schrödinger, LLC, New York, NY, USA). This involved the addition of hydrogen atoms and the assignment of bond orders. Water molecules beyond 5 Å from the ligands were removed. Missing side chains and loops were filled in using Prime. The ionization states of the ligands were determined using Epik at pH 7.0 ± 2.0. Hydrogen bond optimization was conducted, including sampling water orientation, utilizing PROPKA at pH 7.0. Subsequently, hot spot residues on the FGF14/$Na_v1.1$, FGF14/$Na_v1.2$, and FGF14/$Na_v1.6$ complex AF models were identified using Schrodinger Protein Interaction Analysis (Schrödinger, LLC). The SiteMap tool was employed to pinpoint highly ranked potential receptor binding sites in the PPI. A minimum number of site points necessary for definition was established, and the output was restricted to reporting five sites. Grids for all three complexes were created using the Receptor Grid Generation panel, with the centroid of the ligand serving as the center of the grid. Compound 1028 was prepared in its predominant form at pH 7 using the LigPrep panel with the OPLS-2005 force field. Ligand docking was conducted using Glide with the SP protocol. The top conformations of

compound 1028 exhibiting the lowest binding affinity (kcal/mol) were selected for the analysis of binding sites. The docked pose of compound 1028 on the FGF14/$Na_v1.6$ complex was superimposed onto the FGF14/$Na_v1.1$ and FGF14/$Na_v1.2$ models for overlay analysis. All figures were created using Maestro, PyMOL, and ChimeraX.

Animals

Mice. For patch-clamp studies, *Fgf14*$^{-/-}$ mice were maintained on an inbred C57/BL6J background (greater than ten generations of backcrossing to C57/BL6J). All genotypes described were confirmed by Charles River Laboratories International, Inc. (Houston, TX, USA). Wild-type C57/BL6J mice were either *Fgf14*$^{-/-}$ littermates or were purchased from Jackson Laboratory (Bar Harbor, ME, USA). All animal protocols were approved by the UTMB IACUC. For fiber photometry and mouse behavior studies, C57BL/6J mice were acquired from the Jackson Laboratory, and all animal protocols were approved by the US National Institute of Environmental Health Sciences Animal Care and Use Committee.

Rats. All experimental procedures were approved by the Center for Laboratory Animal Medicine and Care of The University of Texas Health Science Center at Houston. The National Institutes of Health guidelines for the care and use of laboratory animals were strictly followed to minimize any potential discomfort and suffering of the animals. Long–Evans hooded adult rats (Charles Rivers Laboratories) 3–5 months of age and weighing 300–450 g at the time of the experiment were used. Rats were single-housed and after a 3-day acclimation period, handled and trained to press a lever for sucrose as described below. Animals were kept in a 12 h light/12 h dark cycle (light from 7:00 to 19:00) and maintained on a restricted diet of 18 g of standard laboratory rat chow provided daily at the end of experimentation. Animals were given *ad libitum* access to water. Animals' weights were monitored weekly to ensure all animals maintained their weight under food restrictions. During the pre-and post-surgery phases, animals were given *ad libitum* access to food for a total of 7 days.

Viral vectors

For patch-clamp studies, AAV2-GFP was purchased from the UNC Vector Core, and AAV2-FGF14^{WT}-GFP and AAV2-FGF14^{R117A}-GFP were designed, constructed, and packaged as previously described[79]. For fiber photometry studies, pAAV-hSyn-mRuby2-GSG-P2A-DA2m was constructed from pAAV-hsyn-GRAB_DA2m (a gift from Yulong Li; Addgene plasmid # 140553; http://n2t.net/addgene:140553; RRID:Addgene_140553)[52] and pAAV-hSyn1-mRuby2-GSG-P2A-GCaMP6f-WPRE-pA (a gift from Tobias Bonhoeffer & Mark Huebener & Tobias Rose; Addgene plasmid # 50943; http://n2t.net/addgene:50943; RRID:Addgene_50943)[80]. The viral vector was recovered in-house by the NIEHS Viral Vector Core, had a titer of 1×10^{13} genome copies per mL, and packaged with AAV9 capsid. For rat behavioral studies, the AAV2-shFGF14-GFP vector was previously described[81].

Stereotaxic surgery

For patch-clamp studies involving stereotaxically injected mice, the stereotaxic injections were performed as previously described[79,81]. For rat behavioral studies, rats were anesthetized with 5% isoflurane in an induction chamber. Animals were positioned in a stereotaxic frame (Kopf Instruments, Tujunga, CA, USA) and anesthesia was maintained with 2.5% isoflurane delivered through a facemask. A heating pad was positioned below the body of the animal, and both temperature and respiration were monitored during the entire surgery. Veterinary lubricant ointment was applied to the eyes to avoid dryness during the surgery. Animals received a subcutaneous injection of the local anesthetic bupivacaine (0.25%, 0.3 ml) at the incision site. Iodine and ethanol (70%) were alternately applied for asepsis of the incision site. The surgery procedures varied according to the type of intracranial implantation/infusion (see below). For injection-only surgeries, the incision was stitched after the infusion by using a surgical suture (Nylon, 3–0). For implantation surgeries, the implants were fixed to the skull using C&B metabond (Parkell, Edgewood, NY, USA), ortho acrylic cement, and four to six anchoring screws. After surgery, animals received a subcutaneous injection of meloxicam (1 mg/kg) and dexamethasone (1 mg/kg), and a topical triple antibiotic was applied to the incision area

Patch-clamp electrophysiology – general

Borosilicate glass pipettes (Harvard Apparatus, Holliston, MA, USA) with resistance of 1.5–3 MΩ (voltage-clamp recordings) or 3–5 MΩ (current-clamp recordings) were fabricated using a PC-100 vertical Micropipette Puller (Narishige International Inc., East Meadow, NY, USA). Recordings were obtained using an Axopatch 200B amplifier (Molecular Devices, Sunnyvale, CA, USA). Membrane capacitance and series resistance were estimated using the dial settings on the amplifier, and capacitive transients and series resistances were compensated by 70–80%. Data acquisition and filtering occurred at 20 and 5 kHz, respectively, before digitization and storage. Clampex 9 software (Molecular Devices) was used to set experimental parameters, and electrophysiological equipment was interfaced with this software using a Digidata 1200 analog-digital interface (Molecular Devices). Analysis of electrophysiological data was performed using Clampfit 11 software (Molecular Devices) and GraphPad Prism 8 software (La Jolla, CA, USA).

Voltage-clamp recordings

HEK293 cell recordings. Cultured cells were dissociated and plated onto glass coverslips at low density. After allowing at least 2 h to ensure cell adhesion, cover slips were transferred to a recording chamber filled with the following extracellular solution: 140 mM NaCl; 3 mM KCl; 1 mM $MgCl_2$; 1 mM $CaCl_2$; 10 mM HEPES; and 10 mM glucose (final pH = 7.3; all salts purchased from Sigma-Aldrich). Cells were incubated with an extracellular solution containing an experimental drug or vehicle for 30 min before beginning recordings. Recording pipettes were filled with an intracellular solution comprised of the following salts: 130 mM CH_3O_3SCs, 1 mM EGTA, 10 mM NaCl; and 10 mM HEPES (pH = 7.3; all salts purchased from Sigma-Aldrich). After GΩ seal formation and entry into the whole-cell configuration, the voltage-clamp protocols shown in Fig. 3f were performed, and acquired electrophysiology data was analyzed as previously described[82].

MSN recordings in brain slices. Acute brain slice preparations were prepared as previously described[82]. After slicing, acute brain slice preparations were transferred from a continuously oxygenated (mixture of 95% O_2/5% CO_2) and chilled tris-based artificial cerebrospinal fluid (aCSF) containing the following salts: 72 mM Tris-HCL; 18 mM Tris-Base; 1.2 mM NaH_2PO_4; 2.5 mM KCl; 20 mM HEPES; 20 mM sucrose; 25 mM $NaHCO_3$; 25 mM glucose; 10 mM $MgSO_4$; 3 mM Na pyruvate; 5 mM Na ascorbate; and 0.5 mM $CaCl_2$ (pH = 7.4 and osmolarity = 300–310 mOsm; all salts purchased from Sigma-Aldrich) to a recovery chamber containing 31 °C cutting solution. After 15 min in the recovery chamber, slices were transferred to a continuously oxygenated and 31 °C chamber containing standard aCSF, which was comprised of the following salts: 123.9 mM NaCl; 3.1 mM KCl; 10 mM glucose; 1 mM $MgCl_2$; 2 mM $CaCl_2$; 24 mM $NaHCO_3$; and 1.16 mM NaH_2PO_4 (pH = 7.4 and osmolarity = 300–310 mOsm; all salts were purchased from Sigma-Aldrich). After at least 30 min of incubation in standard aCSF, slices were incubated for 1 h in either compound or vehicle prior to recordings. After incubation in a compound or vehicle, slices were transferred to a recording chamber perfused with continuously oxygenated and heated standard aCSF (with the caveat that for voltage-clamp recordings, the aCSF was supplemented with 120 μM $CdCl_2$ to block calcium channels). Voltage-clamp recordings of MSNs

were performed using pipettes filled with the following intracellular solution: 100 mM Cs-gluconate (Hello Bio Inc., Princeton, NJ, USA); 10 mM tetraethylammonium chloride; 5 mM 4-aminopyridine; 10 mM EGTA; 1 mM $CaCl_2$; 10 mM HEPES; 4 mM Mg-ATP; 0.3 mM Na_3-GTP; 4 mM Na_2-phosphocreatine; and 4 mM NaCl (pH = 7.4 and osmolarity = 285 ± 5 mOsm/L; CsOH used to adjust pH and osmolarity; all salts except Cs-gluconate purchased from Sigma-Aldrich). After GΩ seal formation and entry into the whole-cell configuration, a cocktail of synaptic blockers (20 μM bicuculine; 20 μM NBQX; and 100 μM AP5 (synaptic blockers purchased from Tocris, Bristol, UK)) was perfused to block synaptic currents. The voltage-clamp protocols shown in Fig. 4a were then performed, and acquired data was analyzed as previously described[82].

Current-clamp recordings

Current-clamp recordings were performed similarly to voltage-clamp recordings in MSNs, with a few differences. Firstly, pipettes with resistance of 3–5 MΩ were used, and the intracellular solution was comprised of the following salts: 145 mM K-gluconate; 2 mM $MgCl_2$; 0.1 mM EGTA; 2.5 mM Na_2ATP; 0.25 mM Na_2GTP; 5 mM phosphocreatine; and 10 mM HEPES (pH = 7.2 and osmolarity = 290 mOsm; all salts were purchased from Sigma-Aldrich). The same aCSF was used as voltage-clamp recordings, except $CdCl_2$ was not added. After GΩ formation and entry into the whole-cell configuration, the amplifier was switched to $I = 0$ mode for approximately 1 min to determine the resting membrane potential before switching to the current-clamp mode to assess intrinsic excitability. During this 1-minute interval in $I = 0$ mode, the same cocktail of synaptic blockers used for voltage-clamp recordings was perfused to halt changes in excitability driven by synaptic activity. The current-clamp protocol shown in Fig. 5a was then employed, and acquired data was analyzed as previously described[82].

Immunocytochemistry (HEK293 cells and mouse tissue)

HEK293 cells were transfected with the respective plasmids and replated on poly-D-lysine coated coverslips for 24 h. The coverslips were washed with PBS and then fixated in 4% PFA for 20 mins. The cells were washed 3x with PBS, permeabilized with 0.3% Triton X-100 for 5 mins, and blocked with a solution containing 3% BSA in PBS + 0.1% Tween-20 for 30 mins. Cells were incubated overnight at 4 °C with primary mouse anti-luciferase (1:300, sc-74548,Santa Cruz Biotechnology) and rabbit anti-CD4 (1:300, ab133313, Abcam, MA, USA) diluted in PBS containing 3% BSA + 0.1% Tween-20. The cells were washed 3x in PBS and incubated with Alexa 488 goat anti-mouse (1:200, A11001, Invitrogen, ThermoFisher Scientific, MA, USA)), Alexa Fluor 647 goat anti-rabbit (1:200, A21245, Invitrogen, ThermoFisher Scientific, MA, USA) and Alexa Fluor plus 405 Phalloidin (1:1000, A30104, Invitrogen, ThermoFisher Scientific, MA, USA)) for 4 h. The coverslips were then washed 3x with PBS and mounted on glass slides with Prolong Gold Antifade reagent (P36934, ThermoFisher Scientific, MA, USA)

Confocal Imaging and Analysis

Confocal images were acquired using a Zeiss LSM-510 Meta confocal microscope with a 63 × oil immersion objective (1.4 NA) in Airyscan mode. Multi-track acquisition was done with excitation lines at 405 nm, 488 nm, and 633 nm. Respective emission filters were band-pass 505–530 nm, band-pass 560–615 nm and low-pass 650. All acquisition parameters, including photomultiplier gain and offset, were kept constant throughout each batch of experiments. Images were analyzed using FIJI (NIH) by selecting ROIs of surface-associated puncta and measuring fluorescence intensity and profiles of the ROIs (Ctrl + M and Ctrl + K). Data were tabulated, normalized using the min/max method, analyzed with Microsoft Excel, and graphed with GraphPad Prism v9.0.

RNA extraction and qRT-PCR analysis

Acute brain slice preparations were prepared with the aid of a UV lamp and lens, the GFP-expressing nucleus accumbens were extracted for RNA isolation. Total RNA was isolated using the RNeasy Mini Plus Kit (Qiagen, France) following the manufacturer's instructions. Total RNA concentrations were quantified using a Nanodrop Spectrophotometer (NanodropTechnologies). Following the RNA quantification cDNA synthesis was performed with 1 μg of total RNA in a 20 μl reaction using the reagents in the iScript cDNA Synthesis Kit (170-8891, Bio-Rad, Hercules, CA, USA) following the manufacturer's instructions. The reaction conditions are as follows: 25 °C (5 min), 46 °C (20 min), and 95 °C (1 min). Real-time qPCR amplifications (performed in duplicate for each sample) were done using 1 μl of cDNA in a total volume of 20 μl using the iTaq Universal SYBR Green Supermix (Bio-Rad, Hercules, CA, USA). The final concentration of the primers was 300 nM. Relative RT-QPCR assays were performed with the GAPDH gene as a normalizer. All qPCR assays were run in the CFX Opus 96 Real-Time PCR System, and the conditions are as follows: 50 °C (2 min), 95 °C (10 min), followed by 40 cycles of 95 °C (15 s) and 60 °C (1 min). The primers used were mouse FGF14 primer (qMmuCED0045683), rat FGF14 primer (qRnoCID0053155), mouse GAPDH primer (qMmuCEP0039581), and rat GAPDH primer (qRnoCID0057018) all purchased from Bio-Rad, Hercules, CA, USA. FGF14 mRNA expression was normalized to GAPDH expression during the analysis of data.

In vivo PK and brain permeability studies

Male Sprague Dawley rats ($n = 3$/group; rats purchased from Beijing Vital River Laboratory, Beijing, China) were intraperitoneally injected with 1028 dissolved in a vehicle (80% saline/15% solutol/5% DMSO) at a dose of 10 mg/kg. Blood samples were collected at designed time points (0.08, 0.25, 0.5, 1.0, 2.0, 4.0, 8.0, and 24 h post-dosing). To determine blood-brain barrier permeability, brain samples were collected at 0.5 h and 1 h post-dosing. The concentration of 1028 in each blood and brain sample was determined by Sundia MediTech Co., Ltd.

Single-unit electrodes implantation

An array of 32 microwires was unilaterally implanted targeting the NAc using the following coordinates from bregma: + 1.2 mm AP, ± 2.3 mm ML, − 7.0 mm DV, 10° angle. The electrodes were customized with the following design: a 2 × 8 grid with 150 μm of space between wires, 200 μm of space between rows, with 35 μm diameter wires (Innovative Neurophysiology Inc, Durham, NC, USA). In all cases, the ground wire was wrapped around a grounding screw previously anchored into the skull. Two insulated metal hooks were implanted bilaterally into the cement to allow firmly attachment of the array connector to the cable during recording.

Viral vector infusion of rats

AAV2-shFGF14-GFP or AAV2-shCTRL-GFP infusions were performed using a micro syringe (SGE, 0.5 μl) with an injection rate of 0.05 μl/min plus an additional waiting time of 12 min to avoid backflow. A volume of 0.5 μl was injected bilaterally into NAc by using the following coordinates from bregma: + 1.4 mm AP, ± 2.3 mm ML, − 7.0 mm DV, 11° angle.

Single-unit electrophysiological recordings in vivo

A 64-channel neuronal data acquisition system (Omniplex, Plexon, Dallas, TX, USA) was used for electrophysiological recordings from freely behaving animals. An electrical isolation Faraday cage was connected to the grounding port of the data acquisition system to reduce 60 Hz noise artifacts. The system was connected to a head-mounted electrode by using a digital headstage cable (32 channels, Plexon), a motorized carrousel commutator (Plexon), and a digital headstage processor (Plexon). Rats were habituated to the headstage cable daily for approximately 1 week before the beginning of the experiments.

Recording chamber. Rats with electrodes previously implanted in the NAc were placed in a plexiglass rectangular arena (40 cm high × 40 cm wide × 26 cm deep, Med Associates, Fairfax, VT, USA) for single-unit recordings. After a 3-minute period of habituation, rats received an intraperitoneal injection of vehicle, and NAc cell activity was recorded for 30 min. After a second baseline period of 3 minutes, rats received an intraperitoneal injection of compound 1028, and NAc cell activity was recorded for an additional 30 min.

Rat lever press training

Rats were placed in a plexiglass standard operant box (34 cm high × 25 cm wide × 23 cm deep, Med Associates) and trained to press a lever for sucrose on a fixed ratio of one pellet for each press. Next, animals were trained in a variable interval schedule of reinforcement that was gradually reduced across the days (one pellet every 15, 30, or 60 s) until the animals reached a minimum criterion of 10 presses/min. All sessions lasted 30 min and were performed on consecutive days. Sucrose pellet delivery, variable intervals, and session duration were controlled by an automated system (ANY-maze, Stoelting, Wood Dale, IL, USA). Lever-press training lasted approximately 7–10 days, after which animals were assigned to surgery or cued food-seeking training.

Rat cued food-seeking training

Rats previously trained to press a lever for sucrose were trained to learn that each lever press in the presence of an audiovisual cue (light: yellow, 2.8 W; tone: 3 kHz, 75 dB; 30-s duration) resulted in the delivery of a sucrose pellet into a nearby dish. The light cue helped to guide the animals toward the lever during the beginning of the training phase, whereas the tone assured that the animals would not miss the trial. After ~ 4 consecutive days of training (24 trials per day, pseudorandom intertrial interval of ~120 s, 60 min session), rats learned to discriminate the food-associated cue as indicated by a significant increase in press rate during the presence of the audiovisual cues, when compared to the 30 s immediately before the cue onset (cue-off). The cued food-seeking training was completed when animals reached 50% of the discriminability index (presses during the cue-on period minus presses during the cue-off period divided by the total number of presses). Reward cue conditioning took place in the same standard operant boxes initially used for lever-press training.

Rat cued food-seeking test

Rats previously trained for audiovisual cue food-seeking were placed in a plexiglass standard operant box (34 cm high × 25 cm wide × 23 cm deep, Med Associates) and tested under restricted or satiated conditions. A total of 16 audiovisual cues (light: yellow, 2.8 W; tone: 3 kHz, 75 dB; 30 s duration) were presented with a pseudorandom intertrial interval of ~120 s, 32 min session. Food-restricted rats were intraperitoneally administrated either vehicle or compound 1028 and immediately placed in the operant boxes. Food-satiated rats with *ad libitum* access to regular chow pellets were given 30 g of sucrose pellets in their home cages 30 min before the test. After free access to sucrose, rats were intraperitoneally administered either vehicle or compound 1028 and immediately placed in the operant boxes. For rats infused with AAV2-shCTRL-GFP l or AAV2-shFGF14-GFP, the same food regimens were adopted, but all the animals were administered with compound 1028 before the tests.

Brain histology for rats

Rats were transcardially perfused with KPBS followed by 10% buffered formalin. Brains were processed for histology as previously described[83]. At the end of the recording sessions, a microlesion was made by passing anodal current (0.3 mA for 15 s) through the active wires to deposit iron in the tissue. After perfusion, rats with electrode implantations had their brains extracted from the skull and stored in a 30% sucrose/6% ferrocyanide solution to stain the iron deposits. Rats infused with viral vectors had their brains extracted and stored in a 30% sucrose KPBS solution. Only rats with the electrode tip locations or the expression of viral vectors in the shell subregion of the NAc were included in the statistical analyses.

Single-unit recording analyses

Extracellular waveforms exceeding a voltage threshold were band-pass filtered (500–5000 Hz), digitized at 40 kHz, and stored on disk. Automated processing was performed using a valley-seeking scan algorithm and then visually evaluated using sort quality metrics (Offline Sorter, Plexon). Single units were selected based on three principal components and waveform features such as valley-to-peak, spike-width, and amplitude measurements. The principal component scores for unsorted waveforms were computed and plotted in a three (or two)-dimensional principal component space. Clusters containing similar valid waveforms were manually defined. After manually clustering similar valid waveforms, a group of spikes were considered from a single neuron if the waveforms formed a discrete, isolated cluster in the principal component space. Commercial software (NeuroExplorer, Nex Technologies, Colorado Springs, CO, USA) was implemented to extract the waveforms and calculate the firing rate of NAc neurons across the recording session.

Behavioral analyses and statistics for rats

Rats were recorded with digital video cameras (Logitech C920) and behavioral responses were measured by using an automated video-tracking system (ANY-maze). Presses per minute were calculated by measuring the number of lever presses during the 30 s cue multiplied by two. The latency to press the lever was calculated by measuring the time the animals spent performing the first lever press after the cue onset. All graphics and numerical values reported in the figures are presented as mean ± SEM. Shapiro–Wilk normality test was performed before the statistical analyses to determine parametrical or non-parametrical statistical tests.

Viral expression of DA2m and mRuby2 control

The viral vector was micro-injected into the medial shell of the nucleus accumbens (NAc) and dorsal lateral striatum (DLS) by standard stereotaxic procedures with animals under isoflurane anesthesia[84]. The coordinates used for targeting NAc were AP + 1.00 mm, ML ± 0.70 mm from Bregma; and DV − 4.00 mm from the brain surface; for DLS were AP + 0.50 mm, ML ± 2.20 mm from Bregma; and DV −2.75 mm from the brain surface. A total volume of 1.0 μl of AAV vector per site was injected at the rate of 0.1 μl per min through a Hamilton Neuros syringe with a 30-gauge needle. The needle was left in place for 10 more minutes before the withdrawal.

Optical fiber probe implantation for in vivo fiber photometry recordings in normal C57BL/6 J mice

Two weeks after the AAV injection, normal C57BL/6 J mice underwent the second stereotaxic surgery to receive fiber probe implantation. Two bur holes were drilled through the skull to target NAc and DLS at two different hemispheres (NAc: AP + 1.00 mm, ML ± 0.50 mm from Bregma; DLS: AP + 0.50 mm, ML ± 2.40 mm from Bregma) using a #1/2 (0.027′ Diameter) drill bit. Another pair of bur holes for anchoring screws were drilled bilaterally above the parietal lobes. After the anchoring screws were in place, a lab-made optical fiber probe, fabricated using a multimode fiber (Thorlabs (Newton, NJ, USA), FG105UCA, NA: 0.22, core diameter: 105 μm, total fiber diameter with cladding: 125 μm, fiber length: flat-cleaved to 2.5 or 4.0 mm after probe assembling and before use) and a ceramic ferrule disassembled from commercial LC connectors (Precision Fiber Products, Inc. (Chula Vista, CA, USA) SKU: MMCON2010, ferrule outer diameter: 1.25, bore diameter: 127 μm)[85,86] was slowly lowered onto the surface of the cortex through the burr hole, then further lowered toward the NAc or DLS at approximately 200 μm per step until the spectra of DA2m and mRuby2 were detected by the spectrometer.

The probe was then lowered at 50 μm per step until the fluorescence intensity reached a plateau. The final tip location was approximately 3.7–3.9 mm for NAc or 1.8–2.2 mm for DLS below the brain surface. The probe was then fixed in place with a generous amount of dental acrylic (Jet, Lang Dental Mfg. Co., Wheeling, IL, USA). The mice were allowed to recover for 2 weeks before experiments proceeded.

Mice operant conditioning

The mice were food-restricted overnight and had access to food 1 h after training every day during operant conditioning training. The operant conditioning training was performed in an open-top mouse operant chamber (21.6 × 17.8 × 12.7 cm, Med-Associates) housed in a sound-attenuating box with 20% sucrose solution as a reward. The training started with a 1 active-lever and 1 inactive-lever, fixed-ratio 1 (FR1) schedule, in which the mice obtained one reward after each active-lever press. Each FR1 session lasted 60 min or until mice received 20 rewards. Once the mice were able to obtain 20 rewards within 30 min, the training would progress to a 1 active-lever and 1 inactive-lever, fixed-ratio 2 (FR2) schedule, in which a total of 2 active-lever presses, were needed for each reward delivery. The training would move on to 1 active-lever and 1 inactive-lever, fixed-ratio 5 (FR5) schedule after the mice could obtain 20 rewards in 30 min in FR2 sessions. Finally, the mice would be then trained in fixed-ratio 10 (FR10) sessions until they could obtain 20 rewards in 30 min.

The mice were trained 6 more days after they obtained 20 rewards in 30 min in FR10 sessions before in vivo fiber photometry recording. The mice were first recorded with food restricted (fasted) and had fully access to food overnight before the second recording (satiated). The mice received i.p. injection of vehicle or 1028 (5 mg/Kg) 10 min before the operant conditioning recording.

The behavior data were recorded with Med-PC V (SOF-736, Med-Associates) and exported with Med-PC to Excel Data Transfer "MPC2XL" Utility (SOF-731, Med-Associates).

Burst analysis on level presses was performed using NeuroExplorer 5 (Nex Technologies). The time stamps of lever presses were imported into NeuroExplorer 5 and analyzed using the "Burst Analysis" function. The "Interval Specifications" settings were set as: max. interval to start burst (sec) = 2; max. interval to end burst (sec) = 5; min. interval between burst (sec) = 5; min. duration of burst (sec) = 1; min. number of spikes in burst = 3. The summary of the numerical results of the burst analysis, including interevent intervals (IEIs) within a burst and inter-burst intervals, was exported to Excel for further analysis

Spectrally resolved fiber photometry

A blue laser (473 nm) was used as the light source to excite both DA2m and mRuby2. Emitted photons were collected by a spectrometer as described previously[53,87]. The in vivo recordings in freely moving mice were carried out in an open-top mouse operant chamber (21.6 × 17.8 × 12.7 cm, Med-Associates) housed in a sound-attenuating box. Fluorescence spectra were acquired using a 19 ms integration time and were triggered by 25 Hz TTL pulses sent from a digital output module (DIG-726TTL, Med-Associates) on a customized mouse operant conditioning package from Med-Associates. Spectral linear unmixing was carried out using a customized program written in R. The customized spectral linear unmixing algorithm script written in R is available at https://www.niehs.nih.gov/research/atniehs/labs/ln/pi/iv/tools/index.cfm. A digital video camera (Grasshopper3GS3-U3-23S6M-C, FLIR Integrated Imaging Solutions (Richmond, BC, Canada), frame by frame triggered by the same TTL pulses triggering the spectrometer, was used to record the mouse's behavior. The output power of the 473 nm laser measured at the end of the patch cable was set at 50 μW.

Immunohistochemistry (fiber photometry and mouse behavior)

Mice were transcardially perfused with phosphate-buffered saline (PBS) followed by 4% paraformaldehyde (PFA). Brains were post-fixed in 4% PFA for 24 h, and then transferred to 30% sucrose in PBS for storage at 4 °C. Coronal slices were sectioned on a microtome (KS34, Thermo Fisher Scientific) at the thickness of 35 μm. Sections were blocked with 10% normal goat serum (S-1000-20, Vector Labs (Newark, CA, USA) and 0.2% Triton X-100 (Sigma) for 1 h at room temperature, followed by incubation at 4 °C overnight with primary antibodies anti-GFP (1:1000, ab13970, Abcam (Waltham, MA, USA) for detecting DA2m. After washing out excessive primary antibodies, the slices were incubated in the secondary antibodies for 2 h at 4 °C. The secondary antibodies used were Alexa Fluor 488 conjugated goat anti-chicken (1:500, A-11039, Invitrogen). After thoroughly washing, the slices were mounted on slides and imaged on a Zeiss Axiocam MR monochrome camera installed on Axio observer Z1 fluorescent microscope with 20x objective (numerical aperture 0.8). The images were acquired and processed using Zen 2012 Blue software (Carl Zeiss, Dublin, CA, USA).

Statistical analysis (fiber photometry and mouse behavior)

The behavior data of operant conditioning were analyzed by Neuroexplorer 5 (Nex Technologies, Lenora, KS, USA). Paired *t* tests were carried out using GraphPad Prism 8 (GraphPad Software). Results of the statistical analyses, including Mean ± SEM, sample sizes, and *P*-values are indicated in either the text or figure legends.

Statistics and reproducibility

For LCA studies, we used sample sizes that were similar to previously published research articles (see Wadsworth et al., 2020, *BBA Mol Cell Res*[30]; Dvorak et al., 2023, *J Neuroinflammation*[81]). Sample sizes for PTS and SPR experiments were similarly pre-determined by referencing previously published research articles (see Wang et al., 2020, *JMC*[31]). Sample sizes for patch-clamp studies were pre-determined by referencing previously published research articles (see Wang et al., 2020, *JMC*[31]; Dvorak et al., 2021, *IJMS*[82]; Dvorak et al., 2023; *J Neuroinflammation*[81]). For in vivo studies, we pre-determined sample sizes by referencing previously published research articles (e.g., Zhou et al., 2021, *Neuropharmacology*[86]). For patch-clamp studies, cells with series resistance > 25 MΩ were excluded. For in vivo studies, animals without correct optical fiber or electrode placement and adequate viral expression were excluded from the study. Samples for LCA experiments, SPR experiments, and patch-clamp studies were fully randomized. For in vivo studies, animals were randomly assigned to experimental or control groups and were tested in a counterbalanced order. For patch-clamp studies, the analysis was not blinded. For in vivo studies, most behavioral data was generated using an automated video tracking software (Any-MAZE).

Reporting summary

Further information on research design is available in the Nature Portfolio Reporting Summary linked to this article.

Data availability

All the data that support the findings presented in this study are included in the Source Data file accompanying the manuscript. Plasmid constructs used in this study were derived from the following clones: FGF14 (NM_175929.2; FGF14 fibroblast growth factor 14 [Homo sapiens (human)] - Gene - NCBI) and $Na_v1.6$ (NM_014191.3; Homo sapiens sodium voltage-gated channel alpha subunit 8 (SCN8A), tra - Nucleotide - NCBI). Data is available from the corresponding author upon request. Source data are provided in this paper.

References

1. Arkin, M. R. & Wells, J. A. Small-molecule inhibitors of protein-protein interactions: progressing towards the dream. *Nat. Rev. Drug Discov.* **3**, 301–317 (2004).
2. Whitty, A. & Kumaravel, G. Between a rock and a hard place? *Nat. Chem. Biol.* **2**, 112–118 (2006).

3. Milroy, L.-G., Grossmann, T. N., Hennig, S., Brunsveld, L. & Ottmann, C. Modulators of protein–protein interactions. *Chem. Rev.* **114**, 4695–4748 (2014).
4. Woollard, S. M. & Kanmogne, G. D. Maraviroc: a review of its use in HIV infection and beyond. *Drug Des. Dev. Ther.* **9**, 5447–5468 (2015).
5. Zi, W. et al. Tirofiban for stroke without large or medium-sized vessel occlusion. *N. Engl. J. Med.* **388**, 2025–2036 (2023).
6. Ivanov, A. A., Khuri, F. R. & Fu, H. Targeting protein-protein interactions as an anticancer strategy. *Trends Pharm. Sci.* **34**, 393–400 (2013).
7. Kitchen, R. R., Rozowsky, J. S., Gerstein, M. B. & Nairn, A. C. Decoding neuroproteomics: integrating the genome, translatome and functional anatomy. *Nat. Neurosci.* **17**, 1491–1499 (2014).
8. Lou, J.-Y. et al. Fibroblast growth factor 14 is an intracellular modulator of voltage-gated sodium channels. *J. Physiol.* **569**, 179–193 (2005).
9. Bosch, M. K. et al. Intracellular FGF14 (iFGF14) is required for spontaneous and evoked firing in cerebellar Purkinje neurons and for motor coordination and balance. *J. Neurosci.* **35**, 6752–6769 (2015).
10. Stanton, C. H., Holmes, A. J., Chang, S. W. C. & Joormann, J. From stress to Anhedonia: Molecular processes through functional circuits. *Trends Neurosci.* **42**, 23–42 (2019).
11. Ali, S. R. et al. Functional modulation of voltage-gated sodium channels by a FGF14-based peptidomimetic. *ACS Chem. Neurosci.* **9**, 976–987 (2018).
12. Alshammari, M. A., Alshammari, T. K. & Laezza, F. Improvedmethods for fluorescence microscopy detection of macromolecules at the Axon Initial Segment. *Front. Cell. Neurosci.* **10**, 5 (2016).
13. Kawaguchi, Y., Wilson, C. J., Augood, S. J. & Emson, P. C. Striatal interneurones: chemical, physiological and morphological characterization. *Trends Neurosci.* **18**, 527–535 (1995).
14. Klawonn, A. M. & Malenka, R. C. Nucleus accumbens modulation in reward and aversion. *Cold Spring Harb. Symp. Quant. Biol.* **83**, 119–129 (2018).
15. Liu, C. et al. An action potential initiation mechanism in distal axons for the control of dopamine release. *Science* **375**, 1378–1385 (2022).
16. Mohebi, A., Collins, V. L. & Berke, J. D. Accumbens cholinergic interneurons dynamically promote dopamine release and enable motivation. *eLife* **12**, e85011 (2023).
17. Gangal, H. et al. Drug reinforcement impairs cognitive flexibility by inhibiting striatal cholinergic neurons. *Nat. Commun.* **14**, 3886 (2023).
18. Yang, H. et al. Nucleus accumbens subnuclei regulate motivated behavior via direct inhibition and disinhibition of VTA dopamine subpopulations. *Neuron* **97**, 434–449 (2018).
19. Castro, D. C. & Bruchas, M. R. A motivational and neuropeptidergic hub: Anatomical and functional diversity within the nucleus accumbens shell. *Neuron* **102**, 529–552 (2019).
20. Willmore, L., Cameron, C., Yang, J., Witten, I. B. & Falkner, A. L. Behavioural and dopaminergic signatures of resilience. *Nature* **611**, 124–132 (2022).
21. Menard, C. et al. Social stress induces neurovascular pathology promoting depression. *Nat. Neurosci.* **20**, 1752–1760 (2017).
22. Krishnan, V. et al. Molecular adaptations underlying susceptibility and resistance to social defeat in brain reward regions. *Cell* **131**, 391–404 (2007).
23. Wadsworth, P. A. et al. High-throughput screening against protein:protein interaction interfaces reveals anti-cancer therapeutics as potent modulators of the voltage-gated Na(+) channel complex. *Sci. Rep.* **9**, 16890 (2019).
24. Arrowsmith, C. H. et al. The promise and peril of chemical probes. *Nat. Chem. Biol.* **11**, 536–541 (2015).
25. Makarenkov, V. et al. An efficient method for the detection and elimination of systematic error in high-throughput screening. *Bioinformatics* **23**, 1648–1657 (2007).
26. Baell, J. B. & Holloway, G. A. New substructure filters for removal of pan assay interference compounds (PAINS) from screening libraries and for their exclusion in bioassays. *J. Med. Chem.* **53**, 2719–2740 (2010).
27. Lipinski, C. A. Drug-like properties and the causes of poor solubility and poor permeability. *J. Pharmacol. Toxicol. Methods* **44**, 235–249 (2000).
28. Wittmack, E. K. et al. Fibroblast growth factor homologous factor 2B: association with Nav1.6 and selective colocalization at nodes of Ranvier of dorsal root axons. *J. Neurosci.* **24**, 6765–6775 (2004).
29. Laezza, F. et al. FGF14 N-terminal splice variants differentially modulate Nav1.2 and Nav1.6-encoded sodium channels. *Mol. Cell Neurosci.* **42**, 90–101 (2009).
30. Wadsworth, P. A. et al. JAK2 regulates Nav1.6 channel function via FGF14(Y158) phosphorylation. *Biochim. Biophys. Acta Mol. Cell Res.* **1867**, 118786 (2020).
31. Wang, P. et al. Design, synthesis, and pharmacological evaluation of analogues derived from the PLEV tetrapeptide as protein–protein interaction modulators of voltage-gated sodium channel 1.6. *J. Med. Chem.* **63**, 11522–11547 (2020).
32. Dvorak, N. M. et al. Bidirectional modulation of the voltage-gated sodium (Nav1.6) channel by rationally designed peptidomimetics. *Molecules* **25**, 3365 (2020).
33. Lu, H. et al. Recent advances in the development of protein–protein interactions modulators: mechanisms and clinical trials. *Signal Transduct. Target. Ther.* **5**, 213 (2020).
34. Ghose, A. K., Herbertz, T., Hudkins, R. L., Dorsey, B. D. & Mallamo, J. P. Knowledge-based, central nervous system (CNS) lead selection and lead optimization for CNS drug discovery. *ACS Chem. Neurosci.* **3**, 50–68 (2012).
35. Rogers, M., Zidar, N., Kikelj, D. & Kirby, R. W. Characterization of endogenous sodium channels in the ND7-23 neuroblastoma cell line: Implications for use as a heterologous ion channel expression system suitable for automated patch clamp screening. *Assay. Drug Dev. Technol.* **14**, 109–130 (2016).
36. Milescu, L. S., Bean, B. P. & Smith, J. C. Isolation of somatic Na+ currents by selective inactivation of axonal channels with a voltage prepulse. *J. Neurosci.* **30**, 7740–7748 (2010).
37. Wang, Q. et al. Ataxia and paroxysmal dyskinesia in mice lacking axonally transported FGF14. *Neuron* **35**, 25–38 (2002).
38. Platkiewicz, J. & Brette, R. A threshold equation for action potential initiation. *PLoS Comput. Biol.* **6**, e1000850 (2010).
39. Wilbers, R. et al. Human voltage-gated Na+ and K+ channel properties underlie sustained fast AP signaling. *Sci. Adv.* **9**, eade3300 (2023).
40. Shah, V. N., Chagot, B. & Chazin, W. J. Calcium-dependent regulation of ion channels. *Calcium Bind Proteins* **1**, 203–212 (2006).
41. Konakov, M. V., Teplov, I. Y., Levin, S. G. & Nenov, M. N. Anti-hypoxic effect of interleukin-10 in hippocampal neurons is mediated by modulation of TASK-1 and TASK-3 channels activity. *Biochem. Biophys. Res. Commun.* **615**, 17–23 (2022).
42. Pablo, J. L. & Pitt, G. S. FGF14 is a regulator of KCNQ2/3 channels. *Proc. Natl. Acad. Sci. USA* **114**, 154–159 (2017).
43. Ali, S. R., Singh, A. K. & Laezza, F. Identification of amino acid residues in fibroblast growth factor 14 (FGF14) required for structure-function interactions with voltage-gated sodium channel Nav1.6. *J. Biol. Chem.* **291**, 11268–11284 (2016).
44. Gardill, B. R., Rivera-Acevedo, R. E., Tung, C.-C. & Van Petegem, F. Crystal structures of Ca(2+)-calmodulin bound to Na(V) C-terminal regions suggest role for EF-hand domain in binding and inactivation. *Proc. Natl. Acad. Sci. USA* **116**, 10763–10772 (2019).

45. Gardill, B. R. et al. The voltage-gated sodium channel EF-hands form an interaction with the III-IV linker that is disturbed by disease-causing mutations. *Sci. Rep.* **8**, 4483 (2018).
46. Gade, A. R., Marx, S. O. & Pitt, G. S. An interaction between the III-IV linker and CTD in NaV1.5 confers regulation of inactivation by CaM and FHF. *J. Gen. Physiol.* **152**, e201912434 (2020).
47. Catterall, W. A. Forty years of sodium channels: Structure, function, pharmacology, and epilepsy. *Neurochem. Res.* **42**, 2495–2504 (2017).
48. Soares-Cunha, C. et al. Activation of D2 dopamine receptor-expressing neurons in the nucleus accumbens increases motivation. *Nat. Commun.* **7**, 11829 (2016).
49. Soares-Cunha, C. et al. Nucleus accumbens microcircuit underlying D2-MSN-driven increase in motivation. *eNeuro* **5**, ENEURO.0386–18.2018 (2018).
50. Crofton, E. J. et al. Glycogen synthase kinase 3 beta alters anxiety-, depression-, and addiction-related behaviors and neuronal activity in the nucleus accumbens shell. *Neuropharmacology* **117**, 49–60 (2017).
51. Sun, F. et al. A genetically encoded fluorescent sensor enables rapid and specific detection of dopamine in flies, fish, and mice. *Cell* **174**, 481–496 (2018).
52. Sun, F. et al. Next-generation GRAB sensors for monitoring dopaminergic activity in vivo. *Nat. Methods* **17**, 1156–1166 (2020).
53. Meng, C. et al. Spectrally resolved fiber photometry for multi-component analysis of brain circuits. *Neuron* **98**, 707–717 (2018).
54. Dvorak, N. M., Wadsworth, P. A., Wang, P., Zhou, J. & Laezza, F. Development of allosteric modulators of voltage-gated Na(+) channels: A novel approach for an old target. *Curr. Top. Med. Chem.* **21**, 841–848 (2021).
55. Fallas, J. A., Dong, J., Tao, Y. J. & Hartgerink, J. D. Structural insights into charge pair interactions in triple helical collagen-like proteins. *J. Biol. Chem.* **287**, 8039–8047 (2012).
56. Yan, H., Pablo, J. L., Wang, C. & Pitt, G. S. FGF14 modulates resurgent sodium current in mouse cerebellar Purkinje neurons. *ELife* **3**, e04193 (2014).
57. Wang, C., Chung, B. C., Yan, H., Lee, S.-Y. & Pitt, G. S. Crystal structure of the ternary complex of a NaV C-terminal domain, a fibroblast growth factor homologous factor, and calmodulin. *Structure* **20**, 1167–1176 (2012).
58. Soares-Cunha, C. et al. Nucleus accumbens medium spiny neurons subtypes signal both reward and aversion. *Mol. Psychiatry* **25**, 3241–3255 (2020).
59. Adeva-Andany, M. M., González-Lucán, M., Donapetry-García, C., Fernández-Fernández, C. & Ameneiros-Rodríguez, E. Glycogen metabolism in humans. *BBA Clin.* **5**, 85–100 (2016).
60. Shavkunov, A. S. et al. The fibroblast growth factor 14·voltage-gated sodium channel complex is a new target of glycogen synthase kinase 3 (GSK3). *J. Biol. Chem.* **288**, 19370–19385 (2013).
61. Floresco, S. B., West, A. R., Ash, B., Moore, H. & Grace, A. A. Afferent modulation of dopamine neuron firing differentially regulates tonic and phasic dopamine transmission. *Nat. Neurosci.* **6**, 968–973 (2003).
62. Hjelmstad, G. O., Xia, Y., Margolis, E. B. & Fields, H. L. Opioid modulation of ventral pallidal afferents to ventral tegmental area neurons. *J. Neurosci.* **33**, 6454–6459 (2013).
63. Mahler, S. V. et al. Designer receptors show role for ventral pallidum input to ventral tegmental area in cocaine seeking. *Nat. Neurosci.* **17**, 577–585 (2014).
64. Descarries, L., Watkins, K. C., Garcia, S., Bosler, O. & Doucet, G. Dual character, asynaptic and synaptic, of the dopamine innervation in adult rat neostriatum: a quantitative autoradiographic and immunocytochemical analysis. *J. Comp. Neurol.* **375**, 167–186 (1996).
65. Gonzales, K. K., Pare, J.-F., Wichmann, T. & Smith, Y. GABAergic inputs from direct and indirect striatal projection neurons onto cholinergic interneurons in the primate putamen. *J. Comp. Neurol.* **521**, 2502–2522 (2013).
66. Bolam, J. P. et al. Substance P-containing terminals in synaptic contact with cholinergic neurons in the neostriatum and basal forebrain: a double immunocytochemical study in the rat. *Brain Res.* **397**, 279–289 (1986).
67. Francis, T. C., Yano, H., Demarest, T. G., Shen, H. & Bonci, A. High-frequency activation of nucleus accumbens D1-MSNs drives excitatory potentiation on D2-MSNs. *Neuron* **103**, 432–444 (2019).
68. Francis, T. C. et al. Nucleus accumbens medium spiny neuron subtypes mediate depression-related outcomes to social defeat stress. *Biol. Psychiatry* **77**, 212–222 (2015).
69. Brideau, C., Gunter, B., Pikounis, B. & Liaw, A. Improved statistical methods for hit selection in high-throughput screening. *J. Biomol. Screen* **8**, 634–647 (2003).
70. Frostell-Karlsson, A. et al. Biosensor analysis of the interaction between immobilized human serum albumin and drug compounds for prediction of human serum albumin binding levels. *J. Med. Chem.* **43**, 1986–1992 (2000).
71. Wang, Y. et al. An experimentally validated approach to calculate the blood-brain barrier permeability of small molecules. *Sci. Rep.* **9**, 6117 (2019).
72. Jorgensen, C., Troendle, E. P., Ulmschneider, J. P., Searson, P. C. & Ulmschneider, M. B. A least-squares-fitting procedure for an efficient preclinical ranking of passive transport across the blood–brain barrier endothelium. *J. Comput. Aided Mol. Des.* **37**, 537–549 (2023).
73. Vanommeslaeghe, K. et al. CHARMM general force field: A force field for drug-like molecules compatible with the CHARMM all-atom additive biological force fields. *J. Comput. Chem.* **31**, 671–690 (2010).
74. Abraham, M. J. et al. GROMACS: High performance molecular simulations through multi-level parallelism from laptops to supercomputers. *SoftwareX* **1–2**, 19–25 (2015).
75. Lippmann, E. S. et al. Derivation of blood-brain barrier endothelial cells from human pluripotent stem cells. *Nat. Biotechnol.* **30**, 783–791 (2012).
76. Jumper, J. et al. Highly accurate protein structure prediction with AlphaFold. *Nature* **596**, 583–589 (2021).
77. Mirdita, M. et al. ColabFold: making protein folding accessible to all. *Nat. Methods* **19**, 679–682 (2022).
78. Ramachandran, S., Kota, P., Ding, F. & Dokholyan, N. V. Automated minimization of steric clashes in protein structures. *Proteins* **79**, 261–270 (2011).
79. Dvorak, N. M. et al. Fibroblast growth factor 13-mediated regulation of medium spiny neuron excitability and cocaine self-administration. *Front. Neurosci.* **17**, 1294567 (2023).
80. Rose, T., Jaepel, J., Hübener, M. & Bonhoeffer, T. Cell-specific restoration of stimulus preference after monocular deprivation in the visual cortex. *Science* **352**, 1319–1322 (2016).
81. Dvorak, N. M. et al. TNFR1 signaling converging on FGF14 controls neuronal hyperactivity and sickness behavior in experimental cerebral malaria. *J. Neuroinflammation* **20**, 306 (2023).
82. Dvorak, N. M. et al. Pharmacologically targeting the fibroblast growth factor 14 interaction site on the voltage-gated Na+ channel 1.6 enables isoform-selective modulation. *Int. J. Mol. Sci.* **22**, 13541 (2021).
83. Do-Monte, F. H., Rodriguez-Romaguera, J., Rosas-Vidal, L. E. & Quirk, G. J. Deep brain stimulation of the ventral striatum increases BDNF in the fear extinction circuit. *Front. Behav. Neurosci.* **7**, 102 (2013).
84. Cui, G. et al. Deep brain optical measurements of cell type–specific neural activity in behaving mice. *Nat. Protoc.* **9**, 1213–1228 (2014).
85. Zhou, J., Li, J., Papaneri, A. B., Kobzar, N. P. & Cui, G. Dopamine neuron challenge test for early detection of Parkinson's disease. *Npj Parkinson's Dis.* **7**, 116 (2021).

86. Zhou, J., Li, J., Papaneri, A. B. & Cui, G. AJ76 and UH232 as potential agents for diagnosing early-stage Parkinson's disease. *Neuropharmacology* **226**, 109397 (2023).
87. Zhou, J. et al. Spectrally resolved fiber photometry for in vivo multicolor fluorescence measurements. *Curr. Protoc.* **2**, e587 (2022).

Acknowledgements

This work was supported by the following: R01 MH132226 (F.L. & J.Z.), S10DO023576 (F.L.), U18DA052504 (F.L.), R01 MH120136 (F.H.D.), R01 MH131570 (F.H.D.), the John D. Stobo, M.D. Distinguished Chair Endowment (J.Z.), the Edith & Robert Zinn Chair Endowment in Drug Discovery (J.Z.), the Houston Area Molecular Biophysics Program Grant No. T32 GM008280 (N.M.D), T32 AG051131 (P.A.W.), Pharmaceutical Research and Manufacturers of America (PhRMA) Foundation Predoctoral Fellowship in Pharmacology/Toxicology (P.A.W.), and T32 ES007254 (C.M.T.). We thank Dr. Paul Smolen (UT Health, Houston, TX) for constructive feedback on the manuscript.

Author contributions

N.M.D. designed and performed patch-clamp studies and LCA studies for 1028, analyzed data, made figures, and wrote the paper; P.A.W. designed and performed LCA, SPR, and PTS for the HTS, analyzed data, made figures, and helped write the paper. G.A., D.S.E., and J.Z. performed in vivo studies with 1028, analyzed data and made figures. P.W. designed and synthesized 1028; N.N. and R.T.P. assisted with the HTS; A.K.S. performed SPR studies. E.P.T and M.B.U. designed and conducted atomic-detail blood-brain barrier permeability simulations for hit compound screening. G.A., C.M.T., and T.J.B. assisted with patch-clamp studies and analyzed data. Z.H. performed molecular modeling of 1028; I.I.S, M.R.A., K.E., Y.M.M.C., P.S., and H.G. assisted with behavioral studies. N.G. and P.L. performed qRT-PCR and confocal imaging studies. M.Z. and H.C. contributed to medicinal chemistry and molecular modeling. Y.A. assisted with electrophysiological experiments and analyzed data. J.S. performed molecular biology. L.K. and J.D. performed stereotaxic injections. A.E.W. performed PTS studies. M.M. analyzed data and helped make figures. T.A.G. supervised behavioral studies and acquired funding for the project. M.D. supervised patch-clamp studies and aided in the interpretation of data. C.S. supervised the HTS and acquired funding for the study. G.C. supervised in vivo studies, edited the paper, and acquired funding for the study. F.H.M. supervised the in vivo electrophysiology and behavioral studies of 1028, edited the paper, and acquired funding for the study. Jia Z. supervised the design and synthesis of 1028 as well as acquired funding for the study. F.L. supervised the HTS and patch-clamp studies, helped make figures and write the paper, and acquired funding for the study.

Competing interests

The corresponding author, F.L., is the founder and president of IonTx Inc., a start-up company focusing on developing regulators of voltage-gated Na^+ channels. The following patent is related to the present study: LAEZ-F-22A: TMB-0170000. Additional information related to the patent is as follows: Patent Int'l Application No: PCT/US24/32688; Title: Non-Peptide Small Molecule FGF14:Nav1.6 Channel Complex Protein-Protein Interaction Modulators; Tech ID: LAEZ-F-22A; Patent Applicant: The Board of Regents of the University of Texas System; Name of the Inventors: Drs. Jia Zhou, Fernanda Laezza, Pingyuan Wang, Nolan M. Dvorak, Paul A. Wadsworth; Status of the Application: Pending; Specific Aspect of the manuscript covered in the patent application: the synthetic route and chemical structure of 1028 is covered in the patent application. All other authors declare that they have no competing interests.

Additional information

Supplementary information The online version contains supplementary material available at https://doi.org/10.1038/s41467-024-55554-7.

Correspondence and requests for materials should be addressed to Fernanda Laezza.

Peer review information *Nature Communications* thanks Chase Francis, who co-reviewed with Desh Deepak Ratna, Dipesh Chaudhury, and the other anonymous reviewers for their contribution to the peer review of this work. A peer review file is available.

Nolan M. Dvorak[1,10], Paul A. Wadsworth[1,2,10], Guillermo Aquino-Miranda[3,10], Pingyuan Wang[1], Douglas S. Engelke[3], Jingheng Zhou[4], Nghi Nguyen[5], Aditya K. Singh[1], Giuseppe Aceto[6,7], Zahra Haghighijoo[1], Isabella I. Smith[3], Nana Goode[1], Mingxiang Zhou[1], Yosef Avchalumov[1], Evan P. Troendle[8], Cynthia M. Tapia[1], Haiying Chen[1], Reid T. Powell[5], Timothy J. Baumgartner[1], Jully Singh[1], Leandra Koff[1], Jessica Di Re[1], Ann E. Wadsworth[1], Mate Marosi[1], Marc R. Azar[9], Kristina Elias[9], Paul Lehmann[1], Yorkiris M. Mármol Contreras[1], Poonam Shah[1], Hector Gutierrez[1],

Thomas A. Green[1], Martin B. Ulmschneider[8], Marcello D'Ascenzo[6,7], Clifford Stephan[5], Guohong Cui[4], Fabricio H. Do Monte[3], Jia Zhou[1] & Fernanda Laezza[1]

[1]Department of Pharmacology and Toxicology, University of Texas Medical Branch, Galveston, TX, USA. [2]Department of Pathology, Stanford Medicine, Stanford, CA, USA. [3]Department of Neurobiology and Anatomy, University of Texas Health Science Center, Houston, TX, USA. [4]Neurobiology Laboratory, National Institute of Environmental Health Sciences, Research Triangle Park, Durham, NC, USA. [5]High-Throughput Research and Screening Center, Texas A&M Health Science Center, Houston, TX, USA. [6]Department of Neuroscience, Università Cattolica del Sacro Cuore, Rome, Italy. [7]Fondazione Policlinico Universitario Agostino Gemelli, IRCCS, Rome, Italy. [8]Department of Chemistry, King's College London 7 Trinity Street, London, UK. [9]Behavioral Pharma Inc., 505 Coast Blvd. South, Suite 212, La Jolla, CA, USA. [10]These authors contributed equally: Nolan M. Dvorak, Paul A. Wadsworth, Guillermo Aquino-Miranda. e-mail: felaezza@utmb.edu